

Subject Code: PPr901

## Shack-Hartmann Based Atmospheric Turbulence Monitor

Submitted to:



Center for Basic Sciences,  
Pt. Ravishankar Shukla University, Raipur (C.G.)

Submitted By:  
**Laxmi Prasoon Barik**  
Roll No. 2010134017

In partial fulfilment of the requirements for the degree of  
Integrated M.Sc. in Physics

under the supervision of

**Dr. Prashant Pathak**  
Assistant Professor,



Space, Planetary and Astronomical Sciences and Engineering (SPASE)  
Indian Institute of Technology, Kanpur  
(2024-25)

(By  
01/02/2025  
(Dr. LAXMI PRASOON)  
(M/S  
01/02/25  
(Dr. MILIND VENKAT))

**DIRECTOR**  
Center for Basic Sciences  
Pt. Ravishankar Shukla University  
Raipur (C. G.) 492 010



# भारतीय प्रौद्योगिकी संस्थान कानपुर

## Indian Institute of Technology Kanpur

अंतरिक्ष, ग्रहीय एवं खगोलीय विज्ञान तथा अभियांत्रिकी विभाग

DEPARTMENT OF SPACE PLANETARY & ASTRONOMICAL SCIENCES & ENGINEERING

### Certificate

This is to certify that the work entitled "Shack-Hartmann based atmospheric turbulence monitor" is a piece of research work done by Laxmi Prasoon Barik under my supervision, from July 2024 to December 2024 towards the fulfillment of his 9th Semester Project (Code-PPr901) of the Integrated M.Sc. program in Physics at Center for Basic Sciences, Pt. Ravishankar Shukla University, Raipur, Chhattisgarh, India.

To the best of my knowledge and belief, this dissertation embodies the work done by the candidate.

I wish him every success in his future academic endeavors.

Dr. Prashant Pathak  
Dated: 03/01/2025  
Place: IIT Kanpur, India

अंतरिक्ष, ग्रह एवं खगोलीय  
विज्ञान एवं अभियांत्रिकी विभाग  
Department of  
Space, Planetary & Astronomical  
Sciences & Engineering  
भारतीय प्रौद्योगिकी संस्थान कानपुर  
INDIAN INSTITUTE OF TECHNOLOGY KANPUR

# Laxmi\_Prasoon\_Barik\_PPr901\_Report.pdf

## ORIGINALITY REPORT



## PRIMARY SOURCES

- |   |   |     |
|---|---|-----|
| 1 | <a href="http://etheses.dur.ac.uk">etheses.dur.ac.uk</a><br>Internet Source   | 7%  |
| 2 | T. Butterley, R. W. Wilson, M. Sarazin.<br>"Determination of the profile of atmospheric optical turbulence strength from SLODAR data", Monthly Notices of the Royal Astronomical Society, 2006<br>Publication | <1% |
| 3 | <a href="http://pure.tue.nl">pure.tue.nl</a><br>Internet Source   | <1% |
| 4 | <a href="http://tel.archives-ouvertes.fr">tel.archives-ouvertes.fr</a><br>Internet Source   | <1% |
| 5 | <a href="http://istina.ipmnet.ru">istina.ipmnet.ru</a><br>Internet Source   | <1% |
| 6 | <a href="http://eprints.usq.edu.au">eprints.usq.edu.au</a><br>Internet Source   | <1% |
| 7 | <a href="http://arxiv.org">arxiv.org</a><br>Internet Source   | <1% |
| 8 | <a href="http://en.wikipedia.org">en.wikipedia.org</a><br>Internet Source   | <1% |

---

## Declaration By The Candidate

I do hereby declare that this project entitled "**Shack-Hartmann Based Atmospheric Turbulence Monitor**" is submitted for the 9th semester Project (PPr-901), Integrated M.Sc. in Physics, Center for Basic Sciences, Pt. Ravishankar Shukla University, Raipur (C.G.), is based on the research work carried out by me under the guidance and supervision of **Dr. Prashant Pathak**, Assistant Professor, Department of Space, Planetary and Astronomical Sciences and Engineering (SPASE) at the Indian Institute of Technology, Kanpur, India.

Date 01/02/2025



Signature of the Candidate

---

## Acknowledgement

I express my sincere gratitude to my project supervisor, **Dr. Prashant Pathak**, Assistant Professor, Space, Planetary and Astronomical Sciences and Engineering (SPASE), Indian Institute of Technology, Kanpur, for giving me the opportunity to work under his esteemed guidance. He has been providing me with great assistance, instructions, and the best accessible information for the project since the first day. Without his patience, guidance, and motivation, this project would not be possible. He made me capable to complete this project and sharpened my skills.

I extend my gratitude, towards **Prof. Kallol K. Ghosh**, Director, Center for Basic Sciences, Pt. Ravishankar Shukla University, Raipur (C.G.), who always supports us to do research.

**Dr. Laxmi Kant**, Assistant Professor, Center for Basic Sciences, Pt. Ravishankar Shukla University, Raipur (C.G.), has always been an inspiration for me in the field of astronomy and astrophysics. He keeps supporting, motivating, and directing me to do my best.

I would like to thank all those who helped me in this research project directly and indirectly. Last but not the least, I am deeply grateful to my parents, and my friends for their best wishes, support, and belief in me.

---

## Abstract

The project focuses on a Shack-Hartmann-based atmospheric turbulence monitor, an advanced tool for atmospheric turbulence monitoring and profiling in astronomical observations. Leveraging a Shack-Hartmann Wavefront Sensor (SHWFS), it measures critical parameters like the Fried parameter ( $r_0$ ) and coherence time ( $\tau_0$ ), offering high temporal resolution and moderate vertical resolution of turbulence. The study incorporates the Kolmogorov and von Kármán turbulence models for generating phase screens, simulates point spread functions (PSFs) using the PROPER optical propagation library, and assesses noise impacts, including photon and read noise. Results demonstrate the atmospheric turbulence monitor's ability to estimate wavefront slopes via photocenter calculations and covariance analysis, providing insights into local turbulence profiles. The portable, cost-effective design enables site assessments and adaptive optics calibration, optimizing telescope performance under real-world conditions.

# Contents

List of Figures . . . . .	vi
List of Tables . . . . .	vii
<b>1 Imaging Under Atmospheric Turbulence</b>	<b>1</b>
<b>2 Atmospheric Turbulence</b>	<b>3</b>
2.1 Introduction . . . . .	3
2.1.1 Kolmogorov Model . . . . .	3
2.2 Scintillation and Seeing . . . . .	5
2.2.1 Seeing Limited Images . . . . .	6
2.3 Seeing Monitors And Turbulence Profilers . . . . .	7
2.3.1 Differential Image Motion Monitor . . . . .	7
2.3.2 Multi-Aperture Scintillation Sensor . . . . .	8
2.3.3 Slope Detection And Ranging . . . . .	8
2.3.4 Scintillation Detection And Ranging . . . . .	10
<b>3 Shack-Hartmann Based Atmospheric Turbulence Monitor</b>	<b>13</b>
3.1 Optical Design and Imaging Parameters . . . . .	13
3.2 Theoretical Calculations . . . . .	14
3.2.1 Estimation of Fried Parameter . . . . .	15
3.2.2 Estimating Photon Counts . . . . .	17
<b>4 Simulation</b>	<b>18</b>
4.1 Phase Screen Generation . . . . .	18
4.2 Fourier Based Approach for Simulation . . . . .	19
4.3 PROPER . . . . .	20
4.3.1 Calculating Photocenter . . . . .	25
4.3.2 Calculating Covariance and Estimating Fried Parameter . . . . .	26
4.3.3 Noise in the PSF . . . . .	27
<b>5 Results and Conclusion</b>	<b>29</b>
5.1 Movement of Centroid . . . . .	29
5.1.1 Statistical Analysis . . . . .	29
5.2 Optimization of the Number of Subapertures . . . . .	32
5.3 Future Directions . . . . .	34
5.4 Conclusion . . . . .	34
<b>Bibliography</b>	<b>38</b>

# List of Figures

1.1 Illustration demonstrating the impact of site selection on image quality. Site A provides a clearer and sharper view of the same object compared to Site B. [25]	1
2.1 Atmospheric conditions, comprising temperature and altitude. Taken from Russell (2009). [11]	3
2.2 An example of how energy is transferred to smaller eddies until smallest scales are reached and energy dissipated by viscosity in eddy breakdown process. [10]	4
2.3 Diagram of the DIMM. Wavefront aberrations are captured by two sub-apertures, focusing light onto two spots that are separated by a distance $x$ on the CCD.	8
2.4 The principle of the Shack-Hartmann Wavefront Sensor (SHWFS) illustrates that shifts in the focused spots produced by the lenslet array correspond to variations in wavefront tilt. Adapted from Platt and Shack (2003) [28].	9
2.5 An illustration of the SLODAR geometry, where $D$ represents the aperture diameter, $h_{\max}$ is the maximum altitude, $\delta h$ denotes the altitude resolution, and $\theta$ is the angular separation between the two stars. Adapted from Perera et al. (2018) [20].	10
2.6 (a) SCIDAR diagram illustrating the detection of two instances of the same wavefront distortion at altitude $h$ , separated by a distance $h\theta$ on the ground, where $\theta$ is the angular separation [26]. (b) Image showing an overlapping pupil pattern used to generate the auto-covariance function. Adapted from Shepherd et al. (2013) [32].	11
3.1 The SHIMM optics schematic. The light is focused onto the CCD at $f_{lenslet}$ after being collimated by the achromatic lens into the lenslet array. Excerpted from Perera et al (2018). [26]	15
4.1 (a) Phase screen for 0.2794 meter aperture with Fried parameter ( $r_0$ ) equals 0.15 m at 550 nm for 512 pixels, (b) Phase screen for 2.794 meter aperture with Fried parameter ( $r_0$ ) equals 0.15 m at 550 nm for 512 pixels.	19
4.2 (a) Primary aperture of 0.2794m with 34 % central obscuration, (b) Simulated PSF using Fast Fourier Transform (fft) based method.	20
4.3 (a) Aperture for an 11 inch with focal ratio 10 at beam diameter fraction of 0.2, (b) Simulated PSF using PROPER.	21
4.4 (a) Phase screen added to the aperture of the primary mirror, (b) PSF after adding the phase screen.	22

---

4.5 (a) An aperture corresponding to a single lens of a lenslet array with $n = 9$ , (b) PSF of the aperture corresponding to the lenslet aperture. . . . .	23
4.6 Aperture divided into $9 \times 9$ grid for a lenslet array of $n = 9$ . . . . .	24
4.7 Phase and PSF of an aperture corresponding to a single lens of a lenslet array. . . . .	24
4.8 Displacement of one spot from the central position due to turbulence. The red cross mark shows the centroid position. . . . .	25
4.9 Spot pattern of SHIMM with 9 subapertures. . . . .	26
4.10 (a) Read noise with amount of 5 electrons and gain of 10 electrons per ADU, (b) Photon noise for the given image. . . . .	28
4.11 (a) PSF with read noise and photon noise, (b) Displaced spot in the pres- ence of noise. . . . .	28
5.1 Comparison of estimated $r_0$ with true value for a total of 500 iterations giving the average percentage error of 2.87%. . . . .	30
5.2 XY Covariance Deviations for All Subapertures Over Time. The thick line is the averaged spot motion for all of the subapertures. Reference methodology adapted from Jacques et al [33]. . . . .	31
5.3 Histogram of RMS Spread of Covariance Deviations (in Arcseconds). . . .	31
5.4 RMS Deviation from Reference vs Separation (X and Y) in Arcseconds. The yellow dotted lines show the corresponding least-squares fitted theo- retical curve for a value of $r_0$ equal to 0.15m. . . . .	32
5.5 SHIMM spot pattern for number of subapertures $n = 6, 9, 12, 15, 20$ ,and 25 respectively. With increase in number of subapertures, the resolution decreases. . . . .	33

# List of Tables

2.1 Comparison of Seeing-Limited and Diffraction-Limited Images . . . . .	6
2.2 Comparison of Turbulence Profilers . . . . .	12
3.1 Comparison of SHIMM with Other Turbulence Profiling Systems . . . . .	17

# Chapter 1

## Imaging Under Atmospheric Turbulence

Due to the dynamic variation in Earth's atmosphere i.e. atmospheric turbulence, the resolving power of ground-based telescopes is limited. This loss of resolution or blur due to turbulence is termed 'seeing'. The wavefront arriving in the Earth's atmosphere can be considered a plane wavefront. Due to the atmospheric turbulence, the wavefront is distorted. To get accurate images, these effects must be considered. The Full Width at Half Maximum (FWHM) of the point spread function (PSF) is a quantitative measure of seeing [2]. PSF is an image of a point source. In other words the PSF is impulse response function (IRF) of a focused optical imaging system.

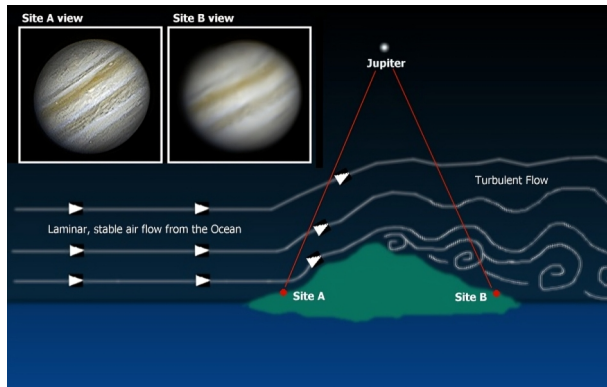


Figure 1.1: Illustration demonstrating the impact of site selection on image quality. Site A provides a clearer and sharper view of the same object compared to Site B. [25]

To construct a larger telescope, it is crucial to understand the atmospheric conditions at the observation site over an extended period, including factors like water vapor content. Long-term monitoring and site surveys provide valuable insights into these conditions, helping to identify optimal locations and refine observational strategies for ground-based telescopes. However, simply collecting the images from a telescope does not involve the factor of atmospheric seeing conditions that affect the measurements. If not accounted for correctly, this can severely affect the observations. This requires characterizing the atmospheric turbulence using various methods and technologies such as using atmospheric turbulence profilers. Upon knowing the seeing conditions, one can compensate for it to improve the observations.

---

Even with an excellent location and ideal conditions, the available observation time remains a critical factor that should not be overlooked, as it significantly influences the quality and effectiveness of imaging.

Wavefront sensing, the technique of detecting an arbitrary wavefront, plays a vital role in imaging and site characterization. By providing precise measurements of atmospheric distortions, it aids in assessing site conditions and improving image clarity, making it an essential component of ground-based telescope operations.

The Shack-Hartmann Wavefront Sensor (SHWFS) is widely used for wavefront sensing. It features a lenslet array positioned in front of a detector, usually a CCD or CMOS camera. As the lens array is traversed by a deformed wavefront, each lenslet focuses the incoming light onto specific spots on the detector. The displacement of these spots correlates to the local slope of the wavefront which enables its reconstruction. SHWFS is valued for its simplicity, robustness, and real-time wavefront measurement capabilities, making it suitable for applications like astronomical imaging and medical sciences.

The pyramid wavefront sensor (PWFS) is another widely used method. It employs a refractive pyramid at the telescope's focal plane, splitting incoming light into four beams directed onto separate detector quadrants. By analyzing the intensity distribution across these quadrants, the wavefront's shape can be inferred. PWFS is highly sensitive to small wavefront errors and performs exceptionally well under low-light conditions. This makes it ideal for high-resolution observations, such as imaging exoplanets and faint celestial objects. However, PWFS requires careful alignment and calibration, adding complexity to its implementation. Curvature sensing measures intensity variations at planes slightly before and behind the telescope's focal plane. The intensity differences reveal the wavefront's curvature, enabling reconstruction. While simple and effective for specific applications, curvature sensors are less sensitive than SHWFS and PWFS and are less commonly used in astronomy. Other methods, such as shearing interferometers and laser-based techniques, cater to specialized scenarios. The choice of sensor depends on the application's requirements and constraints.

While SHWFS performs well with bright guide stars, its efficiency diminishes with faint sources due to reduced signal-to-noise ratio (SNR). Techniques such as laser guide stars and advanced noise reduction algorithms mitigate this limitation.

We utilized a SHWFS for atmospheric characterization. This approach necessitates cameras with extremely high frame rates, which imposes a constraint on the detector's pixel count. Optimizing the number of lenslets is also needed to ensure an acceptable SNR in SHWFS.

# Chapter 2

## Atmospheric Turbulence

### 2.1 Introduction

Atmospheric turbulence occurs when layers of air of different temperatures resulting in different refractive index, mix [13]. It results in ‘scintillation’, which is a variation in intensity, and ‘seeing’, which is a random speckling and movement of the image. [26].

The gradient of refractive index and dynamical turbulence caused by temperature and water vapor results in spatial and temporal fluctuations. They cause phase delays in various wavefront components, which distorts the plane wavefront.

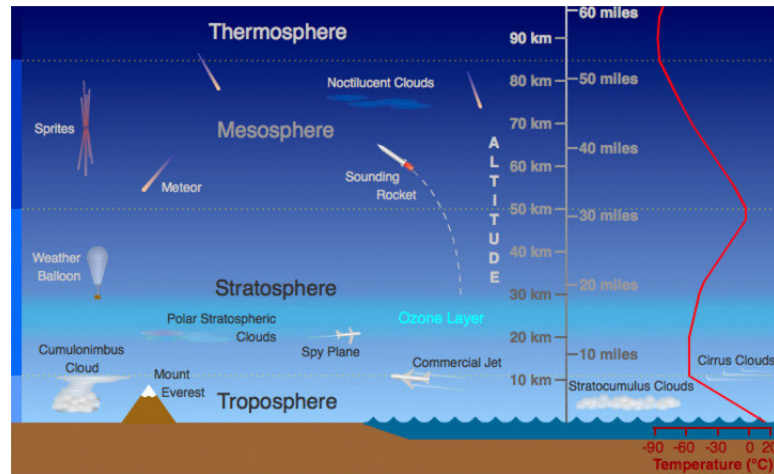


Figure 2.1: Atmospheric conditions, comprising temperature and altitude. Taken from Russell (2009). [1]

#### 2.1.1 Kolmogorov Model

Kolmogorov model is used to describe optical turbulence. It is based on the assumption that energy is introduced into a fluid medium on a large spatial scale, called the outer scale ( $L_0$ ), dissipates to create eddies that get progressively smaller and smaller. This goes on until the medium's viscous characteristics dissipate the turbulence energy at the inner scale ( $l_0$ ), where the Reynolds number  $R_e \approx 1$ .

---

The energy distribution follows a power-law spectrum. Power Spectral Density (PSD) is give by;

$$\Phi(k) \propto k^{-11/3} \quad (2.1)$$

where  $k$  is the wavenumber.



Figure 2.2: An example of how energy is transferred to smaller eddies until smallest scales are reached and energy dissipated by viscosity in eddy breakdown process. [10].

It introduces the term ‘structure-function’, that is turbulence-induced spatial variations in the refractive index.

$$D_n(r) = \langle [n(\epsilon) - n(\epsilon + r)]^2 \rangle, \\ = C_n^2(h)r^{\frac{2}{3}} \quad (2.2)$$

where  $r$  is separation,  $n$  is difference in refractive index, and  $\epsilon$  is the position [15] [30]. The refractive index structure constant,  $C_n^2(h)$ , quantifies the variations in the refractive index. It is employed to assess the turbulence strength of layers at a given height,  $h$ .

The following is a description of the phase structure function:

$$D_\phi(r) = \langle [\phi(\epsilon) - \phi(\epsilon + r)]^2 \rangle, \quad (2.3)$$

As stated by Hardy (1998) [15], for a thin atmospheric layer with Kolmogorov turbulence, the phase structure function is given by:

$$D_\phi(r) = 2.914k^2 \sec(Z)r^{\frac{5}{3}} \int_0^\infty C_n^2(h) dh \quad (2.4)$$

where  $Z$  represents the zenith angle. For small spatial separations, Fried (1965) [11] simplified the equation to:

$$D_\phi(r \ll L_0) = 6.88 \left( \frac{|r|}{r_0} \right)^{\frac{5}{3}}, \quad (2.5)$$

where  $r_0$  is the Fried parameter, which quantifies the integrated turbulence strength. It is related to  $C_n^2(h)$  by:

$$r_0 = \left( 0.423k^2 \sec(Z) \int_0^\infty C_n^2(h) dh \right)^{-\frac{3}{5}} \quad (2.6)$$

where  $k$  is the wavenumber.

---

## Von Kármán Model

von Kármán turbulence model or von Kármán gusts, is a mathematical model of continuous gusts. It first appeared in a 1957 NACA report [9] based on work done by Theodore von Kármán [8].

von Kármán turbulence model extends Kolmogorov turbulence model by including both outer scale ( $L_0$ ) and inner scale ( $l_0$ ) of turbulence. Though its computationally intensive, it is more realistic model than Kolmogorov model because it accounts for the finite sizes of eddies.

Power Spectral Density (PSD) is give by;

$$\Phi(k) \propto \frac{1}{\left(k^2 + \frac{1}{L_0^2}\right)^{11/6}} \quad (2.7)$$

where  $k$  is the wavenumber and  $L_0$  is the outer scale i.e. size of the largest eddies. For large  $k$  (small eddies), the von Kármán model reduces to Kolmogorov behavior.

## Important Parameters

Taking account of the **Fried parameter**, **isoplanatic angle**, and **coherence timescale** is essential.

1. The Fried parameter ( $r_0$ ) characterizes atmospheric optical turbulence by representing the aperture diameter at which the residual phase variance reaches 1 rad<sup>2</sup>.
2. The isoplanatic angle defines the angular separation over which the atmospheric wavefront phase variance remains within 1 rad<sup>2</sup>.
3. The coherence time quantifies how quickly atmospheric turbulence changes over time.

In this study, our primary focus has been on the Fried parameter, commonly referred to as the coherence length.

## 2.2 Scintillation and Seeing

Scintillation is the amplitude distortion of the light waves due to the atmosphere. This affects the brightness of stars and other objects in the sky, as well as the visibility and resolution of astronomical images. Scintillation is commonly observed as the twinkling of stars, where their brightness appears to vary rapidly over short time intervals. Scintillation significantly impacts observations by reducing the clarity, brightness stability, and resolution of images captured through ground-based telescopes. It can introduce noise in photometric measurements, complicating efforts to accurately quantify the luminosity and other properties of celestial objects. For brighter stars and other compact sources, scintillation can be particularly pronounced, while extended sources, like galaxies, are less affected because their light is averaged over a larger area.

Due to optical turbulence, image in a ground-based telescope is blurred known as seeing. Quantitatively, seeing can be measured as the Full Width Half Maximum (FWHM) of the PSF [36]. However, other factors also affect the seeing. The overall strength of the turbulence along line of sight determines seeing. For a better understanding of seeing,

---

the Fried parameter  $r_0$  was defined by Fried [12]. The FWHM of the atmospheric PSF equals:

$$\epsilon = 0.981(\lambda/r_0) \quad (2.8)$$

This is the formal equation for seeing. In reality, what we measure is the turbulence profile because the turbulence is not uniform and stationary. For longer duration, it is more likely that there is variation in the measured quantities.

### 2.2.1 Seeing Limited Images

#### Diffraction Limited Images

A diffraction-limited image achieves sharpest resolution allowed by the optical system's aperture, unaffected by atmospheric distortions. The resolution is determined by wavelength of light ( $\lambda$ ) and aperture diameter ( $D$ ) using Rayleigh criterion;

$$\theta = 1.22 \cdot \frac{\lambda}{D} \quad (2.9)$$

Such images display an Airy disk pattern for point sources, and this quality is typically achieved in space-based telescopes or systems with adaptive optics.

#### Seeing Limited Images

A seeing-limited image is constrained by atmospheric turbulence, which causes light waves to be distorted before reaching the telescope. The resolution in these images is limited by the seeing conditions often ranging from 0.5 to 2 arcseconds. Seeing-limited images accurately represent the real-world conditions under which ground-based telescopes operate, making them essential for calibrating and optimizing adaptive optics systems. By working with seeing-limited images, seeing monitors effectively models the actual limitations imposed by the Earth's atmosphere, providing critical insights for improving ground-based astronomical observations.

Table 2.1: Comparison of Seeing-Limited and Diffraction-Limited Images

Aspect	Seeing-Limited Image	Diffraction-Limited Image
<b>Definition</b>	Limited by atmospheric turbulence.	Limited by the optical system's diffraction.
<b>Resolution</b>	Typically 0.5–2 arcseconds.	$\theta = 1.22 \frac{\lambda}{D}$ , where $\lambda$ is wavelength, $D$ is aperture.
<b>PSF</b>	Blurred, irregular due to turbulence.	Sharp, Airy disk pattern.
<b>Atmospheric Dependence</b>	Strongly affected by turbulence.	Independent of atmospheric effects.
<b>Conditions</b>	Ground-based telescopes without adaptive optics.	Space-based or adaptive optics systems.
<b>Applications</b>	Measuring atmospheric seeing (e.g., SHIMM).	High-resolution imaging (e.g., Hubble, JWST).
<b>Limitations</b>	Blurring reduces detail.	Limited by aperture size and wavelength.
<b>Improvements</b>	Adaptive optics, post-processing, better sites.	Larger apertures, shorter wavelengths.

---

## 2.3 Seeing Monitors And Turbulence Profilers

Currently, several types of seeing monitors and turbulence profilers are being employed across multiple observation sites to improve AO performance, optimize telescope operation and characterize the atmosphere [24] [31] [35] [29] [27] [14] [38]. Seeing monitors observe the overall impact of atmospheric turbulence, while turbulence profilers measure and determine the vertical distribution of turbulence.

### 2.3.1 Differential Image Motion Monitor

The Differential Image Motion Monitor (DIMM) is a tool used to monitor seeing, utilizing a small telescope. It was developed for quantitative evaluation of atmospheric turbulence strength. Its principle is to allow light into the optical system through two small apertures. The differential position of two images formed by the two apertures over time is recorded [24]. The major advantage using this method is that it is insensitive to tracking errors as relative motion of the images are measured [31].

The centroid positions of the two images captured on the detectors can be used to calculate the variance in their differential motion. By measuring the differential motion of a star at zenith distance  $Z$ , the seeing angle of a long-exposure photograph can be determined using the following formula;

$$\theta_{FWHM} = 0.98 \left( \frac{D}{\lambda} \right)^{\frac{1}{5}} \left( \frac{\sigma_*^2 \cos(Z)}{K_*} \right)^{\frac{3}{5}} \quad (2.10)$$

where  $\sigma_*$  denotes the variance in the differential motion, and  $*$  represents either the longitudinal or transverse direction relative to the vector subaperture separation.  $K$  is a constant known as the response coefficient, and  $D$  refers to the subaperture diameter.

The variance can be calculated as;

$$\begin{aligned} \sigma^2 &= \langle |c_1 - c_2|^2 \rangle - \langle |c_1 - c_2| \rangle^2 \\ &= \sigma_{c_1}^2 + \sigma_{c_2}^2 - 2 \text{cov}(c_1 c_2) \end{aligned} \quad (2.11)$$

Where  $c_1$  and  $c_2$  are the centroid values [26]. Strong scintillation causes DIMM to underestimate seeing. There is no turbulence profile or  $r_0$  measured for an individual measurement.

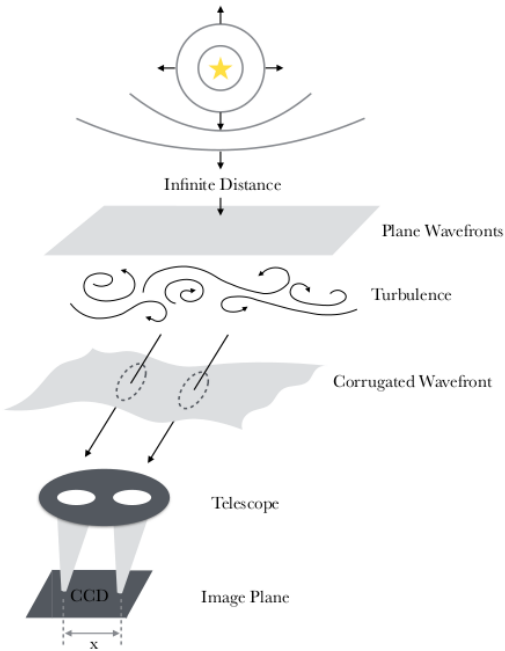


Figure 2.3: Diagram of the DIMM. Wavefront aberrations are captured by two subapertures, focusing light onto two spots that are separated by a distance  $x$  on the CCD.

### 2.3.2 Multi-Aperture Scintillation Sensor

Multi-Aperture Scintillation Sensor (MASS) is a turbulence profiler measuring atmosphere in layers. It does so by analyzing spatial intensity fluctuations measured at the ground [34].

Any turbulence profile can be represented as a collection of several independent layers. Scintillation indices measured by MASS are linear combinations of layer intensities with corresponding weighting functions. From measured indices, layer intensities can be found. Thus resulting in profile restoration. With apertures of different size, one can distinguish the altitude where the scintillation was produced. [17].

Turbulence below 0.5 km is undetected by the MASS because weak scintillation is often hard to distinguish from stronger scintillation that originates at high elevations [34] [35].

### 2.3.3 Slope Detection And Ranging

SLOpe Detection And Ranging (SLODAR) is developed to profile vertical distribution of turbulence,  $C_n^2(h)$  [22].

The wavefront aberrations are used to profile atmosphere. It images a pair of stars with known angular separations using a SHWFS [26]. SHWFS comprises a 2-D array of lenslets with identical focal lengths. Each lenslet focuses an image at a particular spot for a plane wavefront. However, the focus spot deviates from the intended position if there is any distortion in the plane wavefront.

Mathematically, the deviated position is;

$$\delta x = f \cdot \theta_{slope} \quad (2.12)$$

where  $f$  is focal length and  $\theta_{slope}$  is angle of the wavefront slope [28].

Amplitude of this deviation can determine local tip and tilt of wavefront over the sub-aperture. A phase map of wavefront can be reconstructed using measurements of centroid positions of focused spots.

The triangulation method in SLODAR can be used to determine altitude, strength, and velocity of each turbulent layer. Maximum altitude ( $h_{max}$ ) and vertical resolution ( $\delta_h$ ) are determined by the geometry of system. The value of  $h_{max}$  is;

$$h_{max} = \frac{D}{\theta}, \quad (2.13)$$

where  $D$  is telescopic aperture and  $\theta$  is angular separation of target stars. The vertical resolution is expressed by;

$$\delta h = \frac{D}{n\theta} \cdot \cos(Z), \quad (2.14)$$

where  $n$  is number of subapertures subtended across pupil and  $Z$  is zenith angle of observed target [22] [23].

For every target star path, SLODAR estimates the spatial covariance of the gradient of the phase aberration observed at ground level [5].

For systems with measured cross-covariance functions, the turbulence profile can be derived by fitting a series of impulse response functions. In the context of a von Karman turbulence model, these functions represent the covariance shape of a thin atmospheric layer at a given altitude. As described in equation 2.14, the turbulence strength within a specific altitude range is estimated through this fitting process.

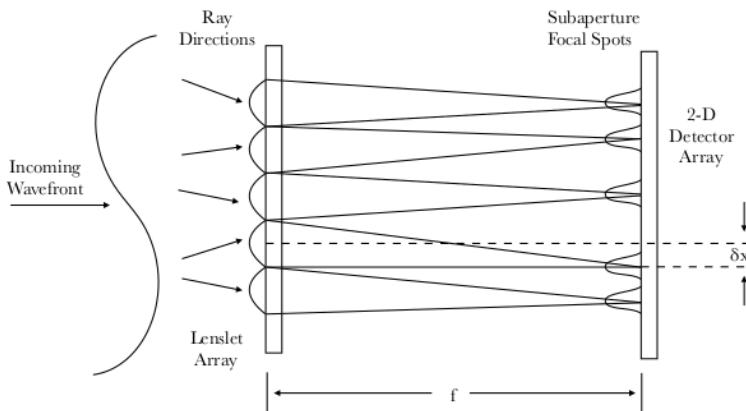


Figure 2.4: The principle of the Shack-Hartmann Wavefront Sensor (SHWFS) illustrates that shifts in the focused spots produced by the lenslet array correspond to variations in wavefront tilt. Adapted from Platt and Shack (2003) [28].

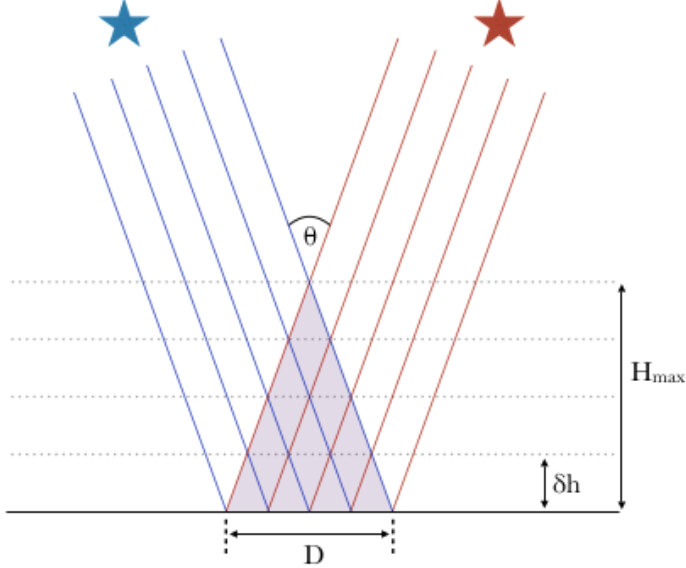


Figure 2.5: An illustration of the SLODAR geometry, where  $D$  represents the aperture diameter,  $h_{\max}$  is the maximum altitude,  $\delta h$  denotes the altitude resolution, and  $\theta$  is the angular separation between the two stars. Adapted from Perera et al. (2018) [26].

### 2.3.4 Scintillation Detection And Ranging

SCIntillation Detection And Ranging (SCIDAR) also makes use of a triangulation technique. A telescopic pupil image is formed on a detector as two stars are seen. The turbulence profile is estimated by analyzing the correlation of scintillation patterns from each star [37] as illustrated in figure 2.6 (a).

A ground-based detector will observe two instances of the same wavefront distortion for a turbulent layer at altitude  $h$ , separated by a distance of  $h\theta$ , where  $\theta$  is the angular separation between the two stars. At a separation corresponding to this distance, this results in a peak in the image's spatial covariance which is averaged over time. The turbulence strength at  $h$  has a relation with correlation peak's amplitude. The temporal cross-covariance map can be used to determine wind velocity. When there is no temporal offset, cross-covariance map forms peaks that represent turbulent layers at various altitudes. These peaks shift throughout the map as offset increases with time. This movement shows the direction and speed at which turbulent layer moves across the telescope aperture.

In SCIDAR, the pupil image is produced onto the same CCD, whereas stereo-SCIDAR uses separate EMCCD detectors for each star [32]. There is an overlap with an offset in the images that is dependednt on angular separation of the two stars. Due to the intensity pattern from each star that correlates with itself and the other star, three peaks are formed for each layer of turbulence in auto-covariance function [32], as shown in figure 2.6 (b).

The theoretical vertical resolution of SCIDAR is determined by the size of the Fresnel radius at a specific altitude by;

---


$$\delta h(z) = 0.78 \frac{\sqrt{\lambda z}}{\theta} \quad (2.15)$$

where  $z = |h - h_{conj}|$  and  $h_{conj}$  is conjugate altitude of the detector [29].

At the zenith, the maximum altitude is described as follows;

$$h_{\max} = \frac{(D - \sqrt{\lambda h_{conj}})}{\theta} \quad (2.16)$$

The combined pupil image loses contrast when the pupil patterns for the two stars superimpose which results in loss of information. Stereo-SCIDAR is modification designed to address this problem. There are other modifications also such as Low Layer SCIDAR (LOLAS) [4]

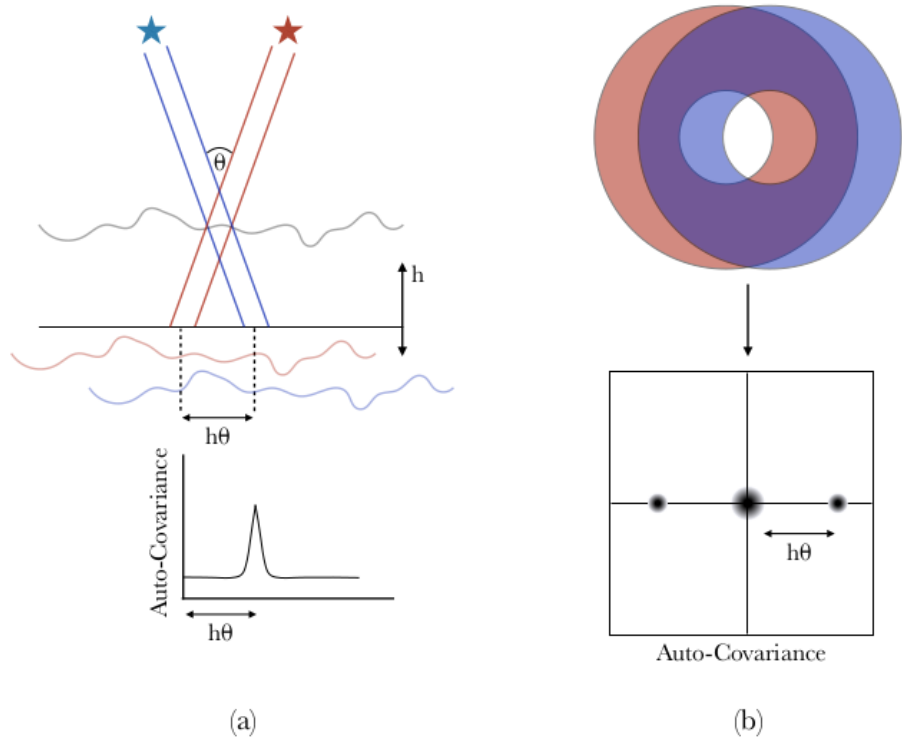


Figure 2.6: (a) SCIDAR diagram illustrating the detection of two instances of the same wavefront distortion at altitude  $h$ , separated by a distance  $h\theta$  on the ground, where  $\theta$  is the angular separation [26]. (b) Image showing an overlapping pupil pattern used to generate the auto-covariance function. Adapted from Shepherd et al. (2013) [32].

Table 2.2: Comparison of Turbulence Profilers

Profiler	Principle	Key Outputs	Resolution	Accuracy	Requirements	Strengths
DIMM	Measures differential image motion between subapertures.	$r_0$ (seeing)	Low vertical, high temporal	Sensitive to noise and wind errors.	Small telescope, aperture mask	Low-cost, portable, simple setup.
MASS	Measures scintillation via multi-aperture mask.	$r_0$ , high-altitude turbulence	Good vertical, poor temporal	Accurate for high altitudes.	Specialized photometer, small telescope	Sensitive to high-altitude turbulence.
SLODAR	Correlates waveform slopes of two stars.	$r_0$ , low-altitude turbulence profile	High vertical, moderate temporal	Detailed low-altitude profiles.	Large telescope, SHWFS	Effective for ground-layer profiling.
SCIDAR	Uses scintillation covariance from two stars.	Turbulence profile, wind speed	High vertical, high temporal	Accurate across altitudes.	Large telescope ( $< 0.5$ m), specialized optics	Comprehensive turbulence and wind profiling.
SHIMM	Shack-Hartmann lenslet array images focused spots.	$r_0, \tau_0$ , turbulence profile	Moderate vertical, high temporal	Corrects scintillation, noise-robust.	Small telescope, SHWFS, fast CCD	Portable, low-cost, measures $\tau_0$ .

# Chapter 3

## Shack-Hartmann Based Atmospheric Turbulence Monitor

### 3.1 Optical Design and Imaging Parameters

One of the Shack-Hartmann based atmospheric turbulence monitor is Shack-Hartmann Image Motion Monitor (SHIMM). It is similar to DIMM, but instead of an aperture mask, it utilizes SHWFS that allows the gathering of more light producing more focused spots. The main objective of SHIMM was to provide a portable, low-cost, and easily replicable seeing monitor. This makes SHIMM ideal for comparing the atmospheric conditions surrounding a large observing site [26]. SHIMM is also capable of estimating coherence time ( $\tau_0$ ) and a low-resolution estimation of turbulence profile. The actual setup used by Perera et al.(2018) [26] comprises a telescope, a detector, Wavefront Sensor (WFS) optics, and a control computer for real time analysis and auto-guiding.

Telescopes used were Celestron CGEM 9.25 inch f/10 and Celestron CGEM 11 inch f/10, with both Schmid-Cassagrain type on VX Mount. WFS optics consisted of an achromatic lens with focal length ( $f_{achromatic}$ ) and a lenslet array with ( $n$ ) number of smaller lenses with individual focal length ( $f_{lla}$ ), each having pitch width ( $d_{pitch}$ ).

The image formed by the primary lens is re-imaged onto the lenslet array, dividing the wavefront into smaller sub-apertures. Each sub-aperture produces a focused spot corresponding to the light received from a specific region of the wavefront. For instance, if a star is observed, its light will create a distinct spot within each sub-aperture. A collimator is used to ensure that incoming light is well-collimated before it reaches the lenslet array, enabling precise focusing and accurate spot formation.

#### Sampling

According to the Nyquist sampling criterion, the FWHM of each spot must span at least two detector pixels. This ensures that the spot profile is adequately resolved, allowing precise centroid determination. If fewer than two pixels cover the FWHM, critical details are lost, leading to undersampling and inaccuracies in wavefront reconstruction. Conversely, excessively small pixels (over-sampling) spread the signal across too many pixels, reducing the SNR without adding useful information. Therefore, the lenslet array's design—specifically the focal length and aperture size—must produce spots appropriately sized relative to the detector's pixel pitch, balancing resolution and sensitivity while capturing the full range of spot displacements caused by wavefront aberrations.

---


$$\Delta x \leq \frac{\text{FWHM}}{2} \quad (3.1)$$

where  $\Delta x$  is the sampling interval (e.g., detector pixel size). This ensures that at least two pixels span the FWHM of the spot for proper sampling. For diffraction-limited systems, FWHM of the spot is proportional to wavelength ( $\lambda$ ) of light and inversely proportional to subaperture size ( $d_{pitch}$ );

$$\text{FWHM} \approx \frac{1.22\lambda f}{d_{pitch}} \quad (3.2)$$

where  $f$  is the focal length of the subaperture.

### Optimizing the Number of Subapertures

Optimizing the number of subapertures in SHWFS is essential for achieving a balance between measurement accuracy, sensitivity, and computational efficiency. Subapertures divide the wavefront into smaller segments, enabling the sensor to capture local slope information. Increasing the number of subapertures enhances the spatial resolution of wavefront measurements, allowing finer details of distortions to be captured, which is crucial in applications like astronomy. However, smaller subapertures reduce the dynamic range, making it difficult to detect large wavefront tilts, as spots may move beyond the detection area. Additionally, smaller subapertures collect less light, leading to a lower SNR, which can degrade measurement accuracy, particularly in low-light conditions. More subapertures also mean increased computational demands, as the number of spots on the detector grows, requiring more processing power for centroiding and wavefront reconstruction. Physical constraints, such as the size of the SHWFS detector and the optical aperture, further limit the number of subapertures that can be practically implemented. The optimal number of subapertures depends on the application's requirements, including the need for high-resolution wavefront measurements, dynamic range, and real-time processing capability. Simulations and experimental tests are often employed to identify the best configuration, ensuring the SHIMM meets the performance and operational constraints of the system.

## 3.2 Theoretical Calculations

For SHIMM, the system design is driven by pre-defined parameters, including CCD format, pixel size of CCD, telescope aperture, f-number (ratio of the focal length by diameter of entrance pupil of the telescope), and the desired number of subapertures across the telescope aperture. These parameters determine the spatial resolution and sensitivity of the SHIMM system. To achieve the correct image scale and the desired number of subapertures, focal length of collimating achromat and focal length and pitch width of the Shack-Hartmann lenslet array must be carefully selected. The collimating achromat ensures that the telescope aperture is appropriately matched to the lenslet array, projecting the wavefront onto the array with the correct scaling. The Shack-Hartmann lenslet array focal length and pitch width control the size and number of subapertures, which directly affect the sampling resolution and image motion sensitivity.

Since these optical components are typically off-the-shelf, available options for their focal lengths and pitches are limited. This often necessitates iterative design adjustments

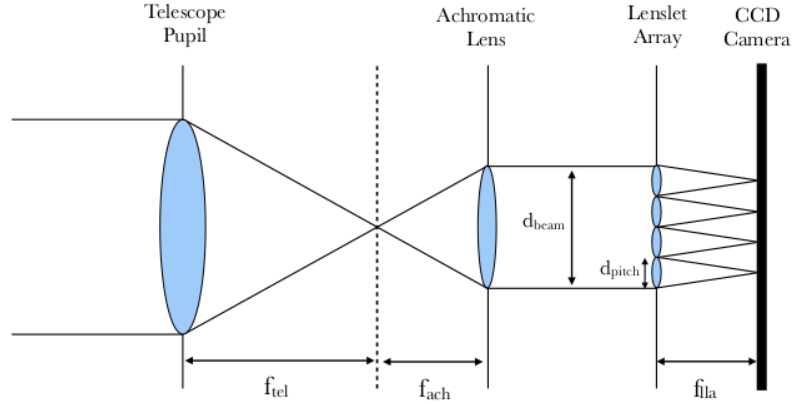


Figure 3.1: The SHIMM optics schematic. The light is focused onto the CCD at  $f_{lenslet}$  after being collimated by the achromatic lens into the lenslet array. Excerpted from Perera et al (2018). [26].

or compromises to align the component specifications with the SHIMM system's performance requirements. Proper selection and alignment of these components are crucial to achieving the desired wavefront sampling and image motion measurements.

The following formulae are used for the calculation;

$$f_{achromatic} = f/\# \times d_{beam} \quad (3.3)$$

where  $d_{beam}$  is defined as

$$d_{beam} = n \times d_{pitch} \quad (3.4)$$

It is essential to know about above parameters to achieve the desired sampling on CCD with the desired number of subapertures ( $n$ ). The schematics is illustrated in [3.1].

### 3.2.1 Estimation of Fried Parameter

The wavefront slope covariance is essential for estimating Fried parameter ( $r_0$ ) under the von Kármán turbulence model. The spatial correlations between wavefront slopes across subapertures reflect the turbulence-induced phase distortions. These correlations are influenced by the separation between subapertures and the atmospheric coherence length. By analyzing the measured covariance of wavefront slopes from displacement of focal spots and fitting them to the theoretical model,  $r_0$  can be accurately determined. This method provides a more comprehensive characterization of atmospheric seeing, accommodating realistic turbulence scales critical for optimizing adaptive optics and site assessment.

The calculation of covariance in SHIMM involves quantifying the relationship between the photocenter displacements of subapertures caused by atmospheric turbulence. For a pair of subapertures, the covariance is determined by evaluating the product of the deviations of their photocenter coordinates (x or y) from their respective means. This process is repeated for all subaperture pairs, and the results are normalized by the total number of pairs to ensure consistency. The calculated covariance provides a statistical measure of the spatial correlation of wavefront slopes between subapertures, which is influenced by strength of atmospheric turbulence and separation between the subapertures.

---

## Calculation of $r_0$ from Covariance

SHIMM utilizes theoretical covariance functions developed for SLODAR [5]. It uses the spatial cross-covariance of wavefront slopes from a SHWFS to infer turbulence strength at different altitudes. The SHWFS measures the wavefront slope across subapertures by analyzing centroid displacements of spot patterns. For SLODAR, observing a double star target allows the separation of contributions from different altitudes due to geometric triangulation. The cross-covariance of wavefront slopes between subapertures, calculated from phase gradients, provides a measure of turbulence strength as a function of altitude. For each turbulent layer at altitude  $H$ , the covariance peak occurs at a spatial offset that is proportional to  $H\theta$ , where  $\theta$  represents the angular separation between the two stars. The altitude resolution is determined by the width of the SHWFS subapertures and the angular separation of the stars, allowing for the quantification of turbulence strength in discrete altitude bins and the construction of a vertical turbulence profile.

SLODAR defines an impulse response function for the SHWFS to model the effect of a thin turbulent layer. By fitting measured covariance data to this theoretical response functions, the turbulence profile ( $(C_n^2(h))$ ) is reconstructed. This profile is then used to compute integrated turbulence metrics such as  $r_0$ . The model also incorporates corrections for noise and biases, such as those arising from telescope tracking errors or atmospheric anisoplanatism. For example, subtracting mean slopes over all subapertures mitigates biases caused by the global tilt.

In the SHIMM, this theoretical framework is adapted to analyze the data.  $r_0$  is calculated by comparing observed covariance values with these modeled theoretical functions. This approach ensures noise-independent measurements and enables SHIMM to achieve accurate seeing characterizations. Thus, the SLODAR-based theoretical model provides the mathematical foundation for the turbulence profiling capabilities of SHIMM.

In order to extract  $r_0$ , the measured spatial auto-covariance ( $cov_{i,m}$ ) is fitted to a theoretical spatial auto-covariance ( $cov_{i,t}$ ) model, based on Kolmogorov's turbulence theory. For the subaperture separation ( $i$ ), the fit can be described as;

$$cov_{i,m} = cov_{i,t} \left( \frac{r_0}{d} \right)^{\frac{-5}{3}} \quad (3.5)$$

Thus, measured auto-covariance can be utilized to estimate  $r_0$  [26]. This estimation provides a quantitative measure of atmospheric turbulence, crucial for understanding its impact on optical observations. By fitting the measured data to the theoretical model, one can assess the coherence length of the atmosphere and optimize systems such as adaptive optics accordingly.

---

### 3.2.2 Estimating Photon Counts

The flux of the source for simulation is calculated using:

$$Flux = 10^{-0.4*m_{app}} * f_0 \quad (3.6)$$

where  $m_{app}$  is apparent magnitude,  $f_0$  means flux at  $m = 0 (Jy)$ , value of  $1Jy = 10^{-23}ergsec^{-1}cm^{-2}Hz^{-1}$  which results in photons;  $1Jy = 1.51 \times photonssec^{-1}m^{-2}(d\lambda/\lambda)^{-1}$ .  $d\lambda/\lambda$  is the ratio of the filter width  $d\lambda$  to the central wavelength  $\lambda$  [7]. (see appendix 5.4 for code implementation)

For example, for an optical system with aperture of primary mirror of 11 inch, secondary obscuration of 34% of primary, flux at  $m = 0$  of 3640 and apparent magnitude of 10 in V-band results 47652 photons per second. The output of simulation is normalized according to the result of this calculation for desired band and magnitude.

Table 3.1: Comparison of SHIMM with Other Turbulence Profiling Systems

Feature	DIMM	MASS	SLODAR	SCIDAR	SHIMM
Measures $r_0$	Yes	Yes	Yes	Yes	Yes
Measures $\tau_0$	No	No	No	No	Yes
Vertical Resolution	Low	Moderate	High	Very High	Moderate
Temporal Resolution	High	Moderate	Moderate	High	High
Low-Altitude Profiling	No	No	Yes	Limited	Yes
Portability	High	Moderate	Low	Low	High
Cost	Low	Moderate	High	High	Low
Ease of Operation	High	Moderate	Moderate	Complex	High

# Chapter 4

## Simulation

### 4.1 Phase Screen Generation

Phase screen is generated using both Kolmogorov and von Kármán turbulence model. The code provided in AOtools allows to generate both a stationary and a moving phase screen that can be applied to an aperture for simulations. It implements the infinite phase screen, as described by Francois, Assemat and Richard W. Wilson in 2006.

The sampling of phase screen can be calculated as;

$$PixelScale_{(phasescreen)} = \frac{D}{GridSize} \quad (4.1)$$

Stationary phase screen is generated with desired sampling. However, for a moving phase screen, it is slightly different. For example,  $D$ , the physical size of the phase screen, 2.794 m and  $GridSize$  of 4096 pixels (used in simulation) results in sampling of  $\approx 6.82 \times 10^{-4} m/pixel$  in case of moving phase screen.

This phasescreen is then cropped to match the size of aperture as it is larger than the aperture size we are simulating for. In the process of cropping, it is ensured that the statistical properties of larger phase screen matches that of cropped part and the sampling remains constant. This is due to the fact that, in AOtools, the inversion of matrices is performed computationally thus limiting the input parameters. Therefore the acceptable parameters are used to ensure the correctness of phase screen generation.

In astronomical imaging, the knowledge about imaging parameters is essential. We have used the primary aperture of 11 inch with focal ratio of 10 for the telescope at 550 nm. During simulation, certain fixed paramters were defined such as grid size for simulation, primary aperture size and obscuration. (see appendix 5.4)

For simulation purpose, the size of primary aperture is taken to be 11 inch ( $\approx 0.2794$  m) for the gridsize 512 x 512 which results in sampling;

$$PixelScale_{(Telescope)} = \frac{diam(m)}{beamratio \times gridsize} \quad (4.2)$$

where  $diam$  is the aperture diameter and beam ratio is beam diameter fraction in comparison to gridsize (=0.8 for simulation). This gives, for the given case, sampling as  $\approx 6.82 \times 10^{-4} m/pixel$  which matches the sampling of phase screen from section 4.1.

For lenslet array, the sampling is  $1.56 \times 10^{-5} m/pixel$  for a gridsize of 64 and beam diameter fraction of 0.3. This means the sampling of lenslet is finer in compared to the primary image, which ensures that it accurately capture the positions of the spots.

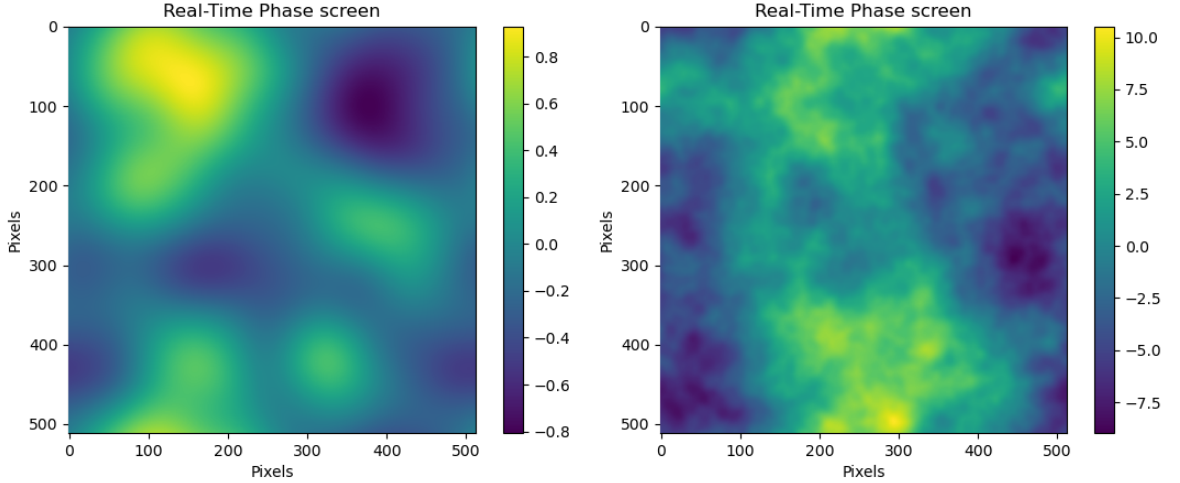


Figure 4.1: (a) Phase screen for 0.2794 meter aperture with Fried parameter ( $r_0$ ) equals 0.15 m at 550 nm for 512 pixels, (b) Phase screen for 2.794 meter aperture with Fried parameter ( $r_0$ ) equals 0.15 m at 550 nm for 512 pixels.

## 4.2 Fourier Based Approach for Simulation

The Fourier-based approach to simulating optical systems is rooted in the principles of Fourier optics, which describe how light interacts with apertures and propagates through an optical system. This approach is particularly effective for modeling diffraction patterns and the PSF of an optical system.

The optical system is defined by its pupil function  $P(x, y)$ , which describes the amplitude and phase of light passing through the aperture at each point  $(x, y)$ . The pupil function incorporates the geometry of the aperture, including features like its shape, size, central obscuration, and any phase aberrations. Mathematically, the pupil function can be represented as:

$$P(x, y) = A(x, y)e^{i\phi(x, y)} \quad (4.3)$$

where  $A(x, y)$  is the amplitude term of the aperture and  $\phi(x, y)$  is the phase term.

The PSF is linked to the pupil function through the Fourier Transform, which models how light propagates from the aperture to the focal plane under the Fraunhofer diffraction approximation. For a monochromatic wave, the complex amplitude  $U(u, v)$  in the focal plane is the Fourier Transform of the pupil function:

$$U(u, v) = \mathcal{F}[P(x, y)] = \int_{-\infty}^{\infty} \int_{-\infty}^{\infty} P(x, y) e^{-i2\pi(ux+vy)} dx dy \quad (4.4)$$

where  $(u, v)$  are the spatial frequencies in focal plane, related to the angles of propagation of the diffracted light.

The PSF represents intensity distribution of light in focal plane and is obtained by taking the squared magnitude of the Fourier transform:

$$\text{PSF}(u, v) = |U(u, v)|^2 = |\mathcal{F}[P(x, y)]|^2 \quad (4.5)$$

It accounts for aperture shape, diffraction, and optical imperfections.

---

The Fourier-based approach is computationally efficient and conceptually straightforward, making it ideal for modeling optical systems where diffraction dominates. It allows direct incorporation of aperture features like central obscurations or spider vanes and can simulate aberrations by modifying the phase term  $\phi(x, y)$  in the pupil function. Additionally, this method is widely applicable in astronomy (e.g., telescope PSFs), microscopy, and adaptive optics systems.

This approach relies on the Fraunhofer diffraction approximation, which assumes far-field propagation. For near-field effects or systems with significant depth variations, alternative methods such as Fresnel diffraction or ray-tracing are required.

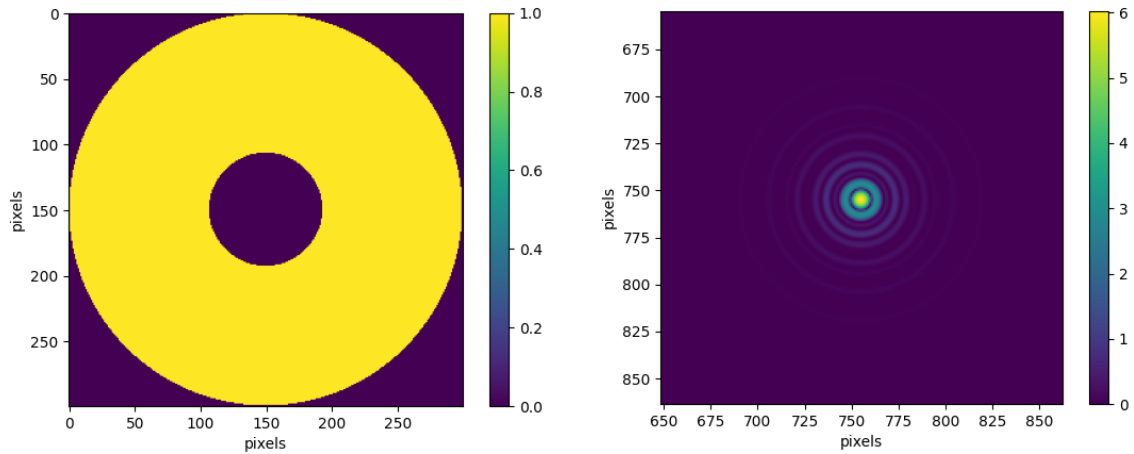


Figure 4.2: (a) Primary aperture of 0.2794m with 34 % central obscuration, (b) Simulated PSF using Fast Fourier Transform (fft) based method.

### Airy Pattern

Even in an ideal optical system, starlight cannot be focused into an infinitely small point. As the light waves converge toward the focal plane, they remain nearly in phase within a region around the geometric focus. Consequently, instead of forming a single point, the light is distributed into a small, bright area known as the Airy disk or diffraction disk. Due to the wave nature of light, some energy extends beyond the Airy disk, creating a faint series of concentric rings, as illustrated in Figure 4.2 (b).

## 4.3 PROPER

The PROPER library for optical propagation is used for simulation [2]. PROPER is a library of routines for Fourier-based wavefront propagation through an optical system. It was developed for modeling stellar coronagraphs at the Jet Propulsion Laboratory [18]. It can also simulate other optical systems concerned with diffraction propagation. In general, there are two methods for simulating the way light propagates through an optical system: (1) Ray tracing, which calculates the trajectory of individual beams, or (2) Physical optics propagation (POP), which calculates variations in the electromagnetic field as the light travels. The latter is used by PROPER.

---

The PROPER library is particularly beneficial for applications that require detailed modeling of diffraction effects and wavefront aberrations in complex optical systems. To propagate a wavefront in near-field and far-field conditions, the PROPER routines utilize common Fourier transform methods. The procedures automatically determine which algorithm to implement based on the pilot beam's characteristics. Both Fresnel and angular spectrum techniques are used in PROPER to ensure accurate wavefront modeling for various optical configurations.

One of the primary applications of PROPER is in the design and simulation of optical systems used in astronomy such as stellar coronagraphs and adaptive optics systems. PROPER is useful to adaptive optics because it simulates how light interacts with wavefront sensors and deformable mirrors. The library can simulate the propagation and correction of wavefront errors resulting from atmospheric turbulence.

A simulation of a PSF using the PROPER can be seen in figure 4.3. The atmospheric turbulence (see fig 4.1(a)) is added to the primary aperture of the telescope. (see appendix 5.4 for code implementation.)

$$d_{\text{airy}} = 2.44\lambda \cdot F/A \quad (4.6)$$

where  $F$  represents focal length and  $A$  denotes aperture size.

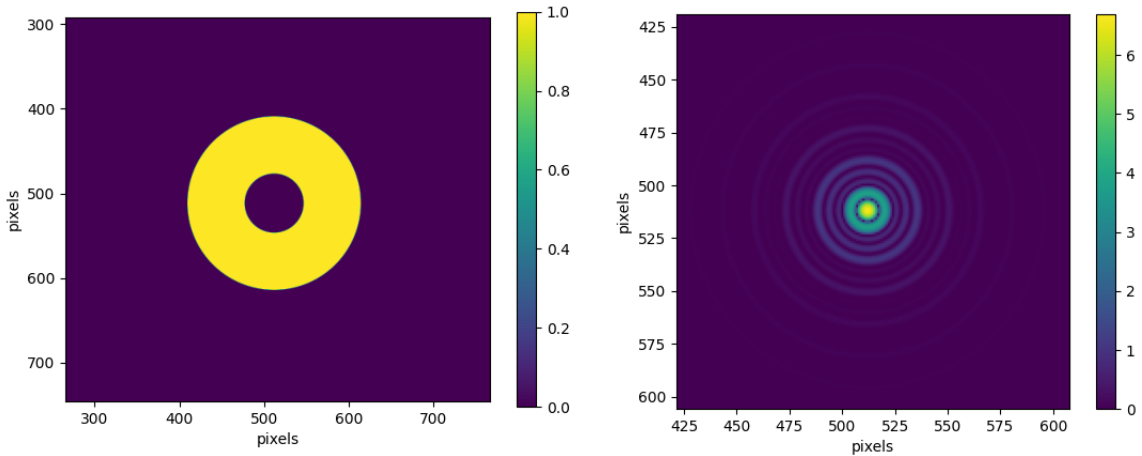


Figure 4.3: (a) Aperture for an 11 inch with focal ratio 10 at beam diameter fraction of 0.2, (b) Simulated PSF using PROPER.

## Resizing

In the simulation, resizing the wavefront to match the size of a lenslet is a crucial step to ensure accurate modeling of the wavefront's interaction with the lenslet array. The process involves extracting a portion of the wavefront corresponding to a specific subaperture and then resizing it according to the beam ratio, which defines the relative size of the wavefront for the simulation grid and the optical system. Resizing is important because it ensures that the extracted portion of the wavefront appropriately matches the dimensions of the lenslet. If the wavefront segment is not properly resized, it can lead to mismatches between the physical optics of the system and the numerical simulation, resulting in errors in the calculated PSF for each subaperture. By scaling the wavefront to the correct size, the

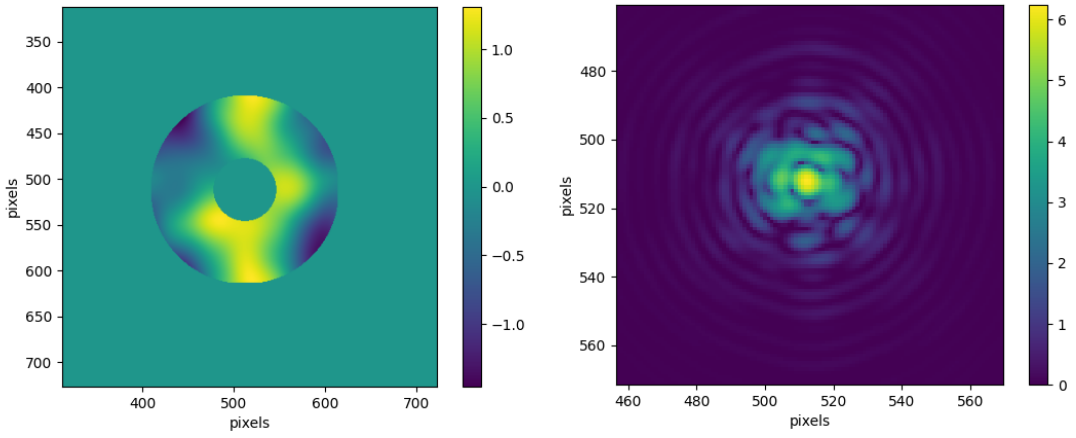


Figure 4.4: (a) Phase screen added to the aperture of the primary mirror, (b) PSF after adding the phase screen.

simulation maintains consistency with the beam size and resolution requirements of the lenslet, allowing the wavefront's local curvature and tilt to be accurately represented.

Additionally, resizing ensures that the numerical grid resolution of the wavefront matches the simulation's requirements for computational efficiency and accuracy. It prevents over-sampling or under-sampling, which could either waste computational resources or lead to loss of critical information about the wavefront's features. Once resized, the wavefront segment is padded to the desired grid size to prepare it for Fourier transforms or further processing, ensuring artifact-free calculations and accurate optical modeling.

## Padding

Padding plays a crucial role in ensuring computational accuracy and minimizing artifacts. Padding involves increasing the size of the computational grid by adding zeros around the optical field prior to performing Fourier transforms. This process minimizes edge effects by preventing the wavefront's edges from wrapping around during the transforms, which could introduce artifacts into the PSF. Additionally, padding improves the sampling resolution in the Fourier domain, enabling the accurate representation of fine details in the PSF. It also reduces aliasing by ensuring that the computational grid is sufficiently large to prevent overlapping of frequency components. Furthermore, padding is essential for accurate far-field calculations, as it ensures the full angular extent of the diffraction pattern is captured without truncation. By zero-padding the wavefront array to a larger size, PROPER achieves enhanced computational precision, producing PSFs that are free from numerical artifacts and suitable for high-accuracy optical simulations.

## PSF for Different Aperture Shapes

The shape of the PSF varies across subapertures because the light entering each sub-aperture corresponds to a different portion of the incoming wavefront. Distortions in the wavefront, caused by atmospheric turbulence, optical misalignments, or imperfections in the telescope optics, result in variations in phase and amplitude of the light sampled by each lenslet in the array. Each lenslet focuses light from its corresponding subaperture onto the detector, forming a spot whose shape and position depend on the local curvature

---

and tilt of the wavefront. For instance, a planar wavefront produces sharp, centered spots, whereas a distorted wavefront leads to shifted or deformed spots. Consequently, the PSFs across subapertures differ in size, shape, and position, encoding the local wavefront distortions. By analyzing these spot variations, the SHWFS can be used to reconstruct the overall wavefront by measuring the local slopes or gradients across aperture.

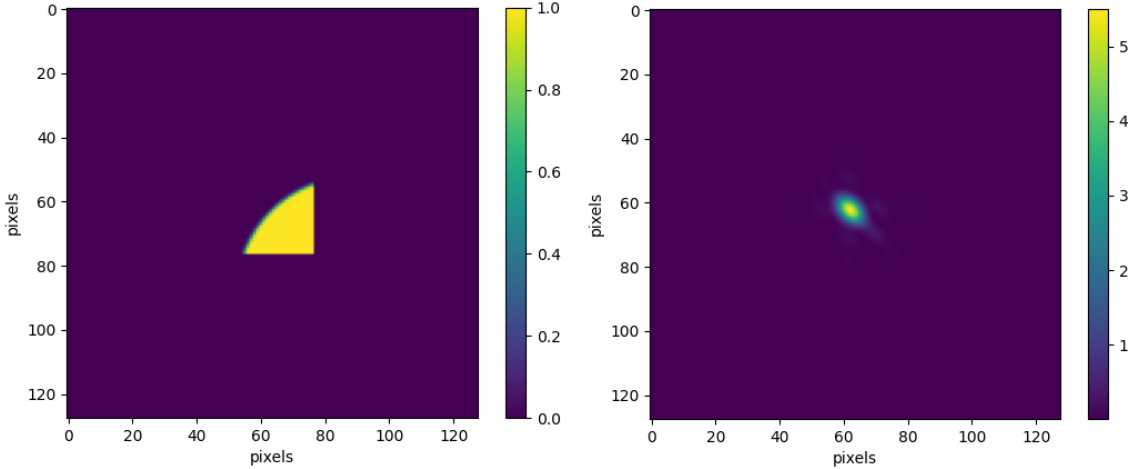


Figure 4.5: (a) An aperture corresponding to a single lens of a lenslet array with  $n = 9$ , (b) PSF of the aperture corresponding to the lenslet aperture.

In SHWFS, the pupil aperture is divided into smaller regions by a grid of lenslets, each corresponding to a sub-aperture that measures the local wavefront slope. The mapping of different parts of the aperture into these sub-apertures depends on the aperture's geometry and any obstructions. For a circular pupil, sub-apertures fully inside the pupil receive complete light and provide reliable measurements. However, sub-apertures near the edge of the pupil, which partially overlap the circular boundary, collect light only from the portions within the aperture, leading to reduced sensitivity and possibly less accurate measurements. Sub-apertures outside the pupil, or in regions obscured by elements like a telescope's secondary mirror, do not receive light and remain inactive. When the sub-apertures are arranged in a uniform rectangular grid, this mismatch between the grid and the circular aperture introduces further variations, especially near the edges. In some designs, adaptive grids, such as hexagonal patterns, are used to better match the aperture shape and reduce these discrepancies. The effective mapping of sub-apertures significantly influences the accuracy of wavefront measurements and calculations, such as the covariance matrix, as irregular mappings introduce variations in sensitivity and noise across the sensor.

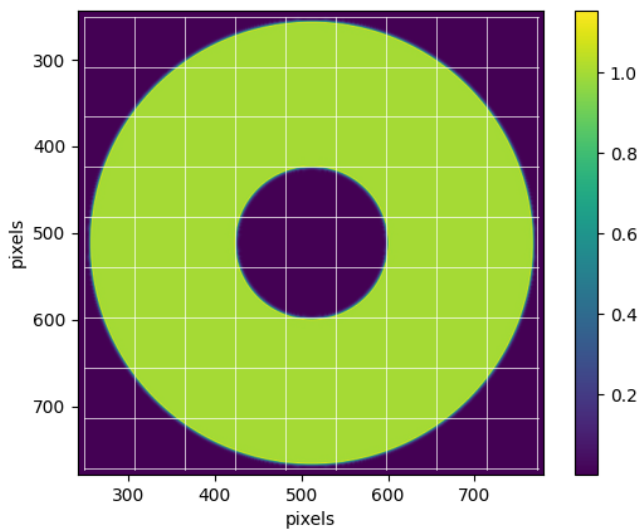


Figure 4.6: Aperture divided into  $9 \times 9$  grid for a lenslet array of  $n = 9$ .

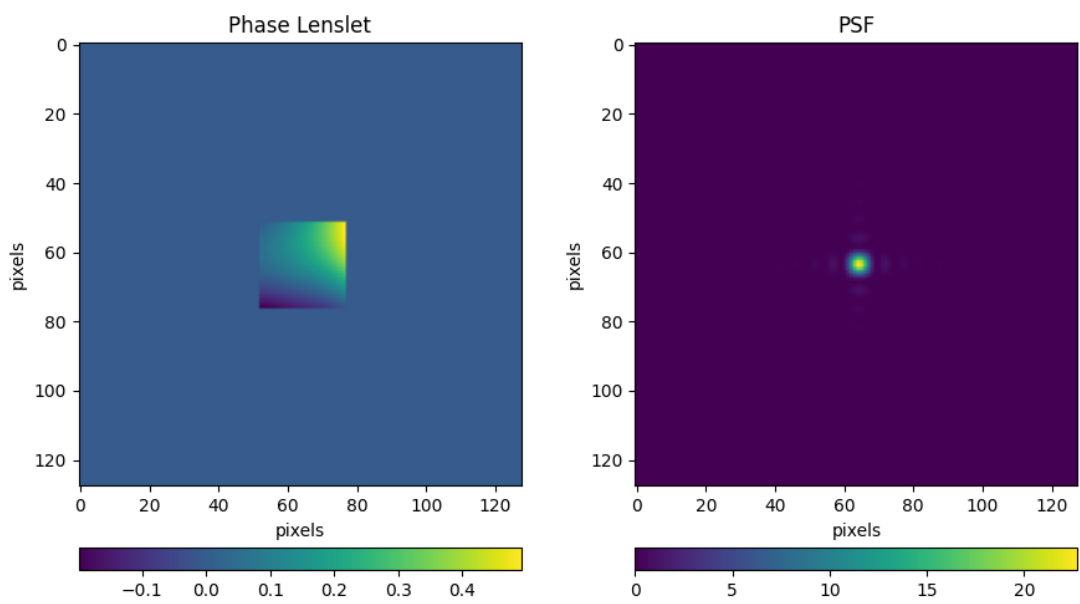


Figure 4.7: Phase and PSF of an aperture corresponding to a single lens of a lenslet array.

### 4.3.1 Calculating Photocenter

The calculation of the photocenter of spots SHIMM is crucial for accurate wavefront analysis and image motion monitoring. The photocenter provides a reliable measure of spot displacement, which directly corresponds to the wavefront slope within each subaperture. This method is less sensitive to noise and detector imperfections compared to simply locating the point of maximum intensity, ensuring robustness under varying conditions. Additionally, during the alignment and calibration of the SHIMM system, photocenter positions help establish reference points and detect systematic offsets or misalignments, enabling precise system optimization.

Calculation of photocenter can be done with a simple center of mass finding algorithm;

$$c_x = \frac{\sum_{x,y} y \cdot I(x,y)}{\text{Total}}, \quad c_y = \frac{\sum_{x,y} x \cdot I(x,y)}{\text{Total}} \quad (4.7)$$

where  $I(x, y)$  is the total intensity.

We can define a function, `photocenter(image, t=0.1)` (see appendix 5.4 for code implementation), to compute the photocenter or centroid of an intensity distribution, such as the focal spot in SHIMM. The function begins by calculating the 99.95th percentile intensity of the image to identify the peak brightness region while ignoring potential outliers. A threshold, determined as a fraction ( $t$ ) of this peak intensity, is then subtracted from the entire image. Pixels below zero are set to zero, effectively isolating the brighter core of the spot while minimizing the influence of background noise. The total remaining intensity is computed, and coordinate grids corresponding to the pixel indices are generated. The photocenter coordinates ( $c_x, c_y$ ) are determined using intensity-weighted averages of the pixel positions, ensuring that brighter regions contribute more to the centroid location. These coordinates are then rounded to integers and returned. This process is crucial for accurately determining the position of the focal spot, which is used to measure local wavefront slopes in SHIMM and assess image motion or wavefront distortions.

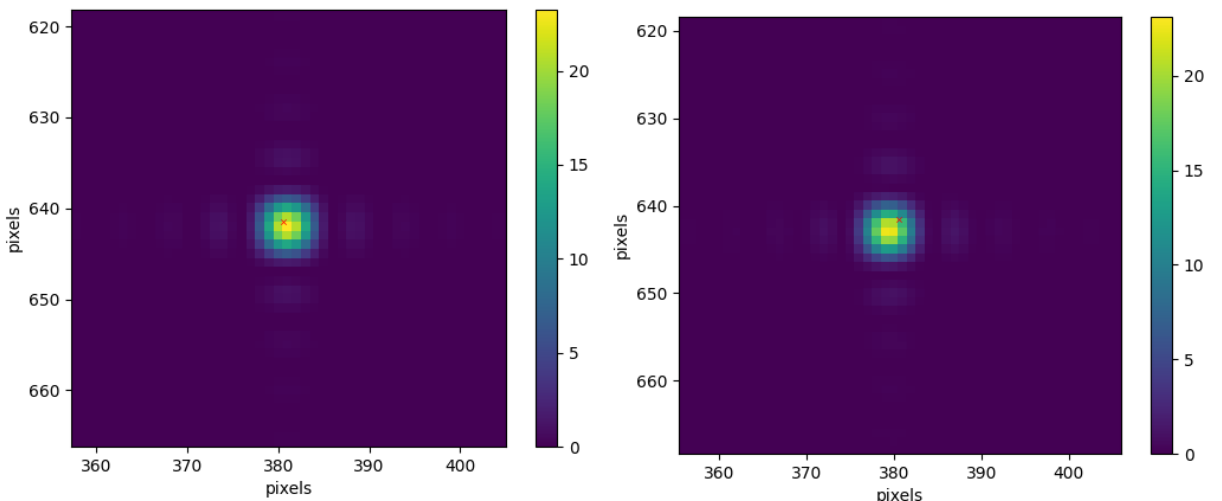


Figure 4.8: Displacement of one spot from the central position due to turbulence. The red cross mark shows the centroid position.

### 4.3.2 Calculating Covariance and Estimating Fried Parameter

The covariance for the simulation can be calculated as;

$$Cov_{(X,Y)} = \frac{1}{n-1} \sum_{i=1}^n (X_i - \bar{X})(Y_i - \bar{Y}) \quad (4.8)$$

where  $X_i$  and  $Y_i$  are  $i$ th observations of  $X$  and  $Y$ . This is the cross-covariance of  $X$  and  $Y$ . For the code implementation (see appendix 5.4), the inputs should include arrays containing the photocenter coordinates ( $X$  and  $Y$ ) for both cases: with phase screen (considered as mean) and without the phase screen, as well as the total number of subapertures. The values  $(X_i - \bar{X})$  and  $(Y_i - \bar{Y})$  give auto-covariance of  $X$  and  $Y$  respectively.

Provided theoretical auto-covariance,  $r_0$  can be estimated using the equation 3.5. If the aperture size is  $D$ , then;

$$r_0 = \left( \frac{\text{observed\_cov}}{\text{theoretical\_cov}} \right)^{-\frac{3}{5}} \cdot D \quad (4.9)$$

The setup in figure 3.1 is simulated which results in spot pattern depending of the number of subapertures used (fig 4.9). In the presence of turbulence, the spots shows a movement (fig 4.8) which can be used to calculate the local slope of the subaperture image.

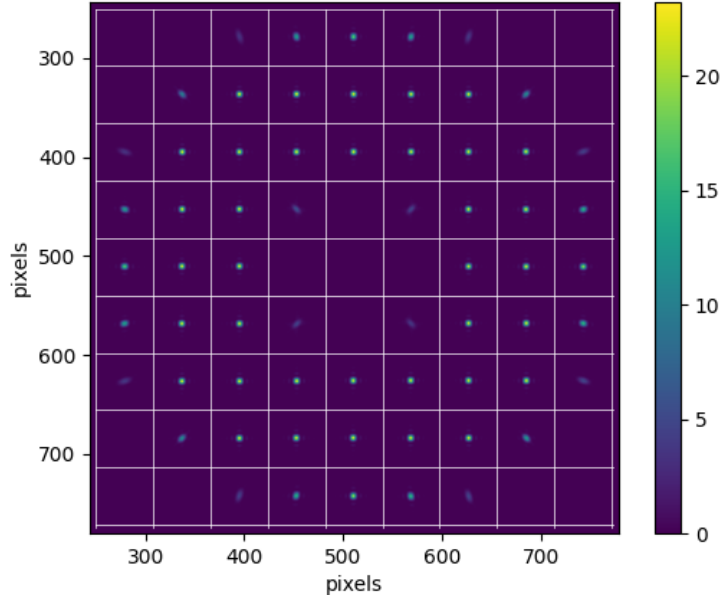


Figure 4.9: Spot pattern of SHIMM with 9 subapertures.

---

### 4.3.3 Noise in the PSF

Image noise is defined as random variations in color information or brightness within the images. Noise is undesirable since it can obscure important details and degrade the overall quality. By simulating the imperfections present in real-world circumstances, noise can improve realistic depiction in simulations.

Depending on the imaging equipment, noise might come from several sources. Noise in digital cameras or sensors is frequently caused by heat factors, electronic interference, or photon detection limitations. Typical noise types include shot noise, which comes from random variations in photon arrivals, readout noise, which is introduced during signal processing in imaging systems, and Gaussian noise, which is uniformly dispersed throughout the image.

#### Read Noise

Read noise refers to the noise introduced by the electronics during the process of transferring charge from the pixels. It is given in electrons which can be converted into counts. Read noise is important because it can limit the resolution of an image. The higher the read noise, the lower the resolution of the digital image. Read noise is incorporated into the simulation of spots to enhance the realism of the system.

#### Photon Noise

Photon noise, also known as shot noise or quantum noise, arises from the inherent natural variations in the incident photon flux due to the statistical nature of electromagnetic waves. This randomness in the signal, caused by the arrival of photons at the detector, follows a Poisson distribution, hence the name Poisson noise. Notably, photon noise has a square root relationship with the signal. Photon noise is typically measured in units of standard deviations, and it can be reduced by increasing the power of the light source or by using a larger detector area. Furthermore, techniques such as averaging can also be used to reduce photon noise.

The simulated PSF with added noise represents a more realistic scenario, as it accounts for imperfections present in real-world observations. Noise introduces variability that mimics the limitations of detectors and environmental factors, providing a closer approximation to actual data. This approach is essential for testing and optimizing algorithms designed for tasks such as image reconstruction or wavefront sensing. By incorporating noise, simulations can evaluate the robustness and reliability of methods under practical conditions, ensuring better performance in real applications. Moreover, it allows for a deeper understanding of how noise impacts the precision and accuracy of measurements. (See appendix 5.4 for code implementation for read-noise and photon noise.)

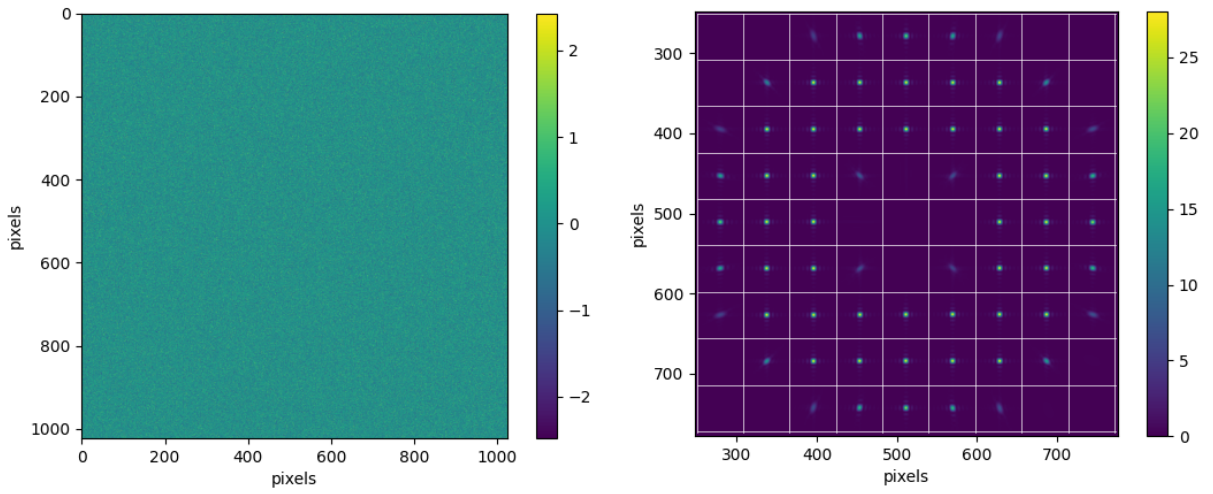


Figure 4.10: (a) Read noise with amount of 5 electrons and gain of 10 electrons per ADU,  
(b) Photon noise for the given image

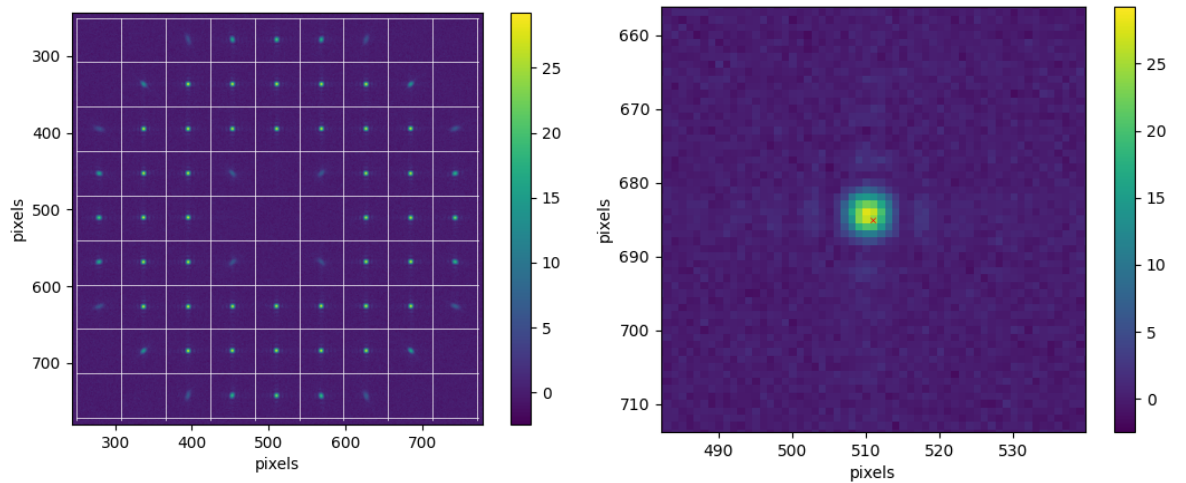


Figure 4.11: (a) PSF with read noise and photon noise, (b) Displaced spot in the presence of noise

# Chapter 5

## Results and Conclusion

### 5.1 Movement of Centroid

SHIMM demonstrates its effectiveness in monitoring atmospheric turbulence by analyzing the movement of spots across subapertures. Simulations conducted using the von Kármán turbulence model successfully generated phase screens that replicate realistic atmospheric conditions, highlighting the versatility of SHIMM for different observing environments. By detecting photocenter displacements in these spots, SHIMM calculates the wavefront slopes, which are integral to deriving the Fried parameter. This parameter serves as a critical measure of atmospheric turbulence strength, directly influencing optical resolution and image quality.

Compared to existing systems like DIMM or MASS, SHIMM offers significant advantages. DIMM, while effective in measuring the Fried parameter, lacks the capability to assess coherence time and is sensitive to tracking errors. MASS, on the other hand, provides turbulence profiling but struggles with low-altitude turbulence detection. SHIMM combines the strengths of these systems and overcomes their limitations by using a SHWFS for real-time turbulence analysis. This enables SHIMM to measure both the Fried parameter ( $r_0$ ) and coherence time ( $\tau_0$ ) accurately, enhancing its utility for diverse applications.

SHIMM's robustness against noise, including photon and read noise, ensures the accuracy of measurements even under challenging conditions. Techniques such as resizing and padding, applied to simulated PSFs, guarantee computational precision and minimize artifact errors. Additionally, the system's compact design and modular approach make it highly portable and cost-effective, allowing for easy deployment across multiple observing sites. This adaptability enhances the role of our technique in site characterization and AO calibration, enabling real-time optimization of telescope performance.

#### 5.1.1 Statistical Analysis

For multiple iterations, the code is modified to use the input from files stored as fits format and return  $r_0$ . For a simulation done for independent phase screens with initial  $r_0$  equals 0.15m,  $L_0$  of 100m,  $l_0$  of 0.1m and a given theoretical covariance value of 0.1,  $r_0$  and observed covariance is given as;

```
|| Mean of observed_covariance for 500 frames: 0.05555555555555555  
|| Average r0: 0.14569488494955998
```

---

Which gives the percentage error of 2.87%. Similarly, for moving phase screens (as used in AOtools) for 90 iterations, and theoretical covariance of 1, this gives;

```
Von Karman Model:
Mean of observed_covariance: 1.0
Average r0: 0.18272016853399045
```

```
Kolmogorov Model:
Mean of observed_covariance: 3.25
Average r0: 0.12745312948081405
```

Which gives the percentage error of  $\approx 21\%$  for Von Karman model. For kolmogorov model, the result gives the percentage error of  $\approx 15\%$ .

The statistical accuracy of  $r_0$  estimation improves with an increasing number of simulation frames, as evidenced by the decreasing variability observed in the graph (Figure 5.1). For more than 200 iterations, this approaches to a constant region. The parameters for the simulation are:  $L_0 = 100m$ ,  $l_0 = 0.1m$ ,  $r_0 = 0.15m$ , and  $n = 6$ .

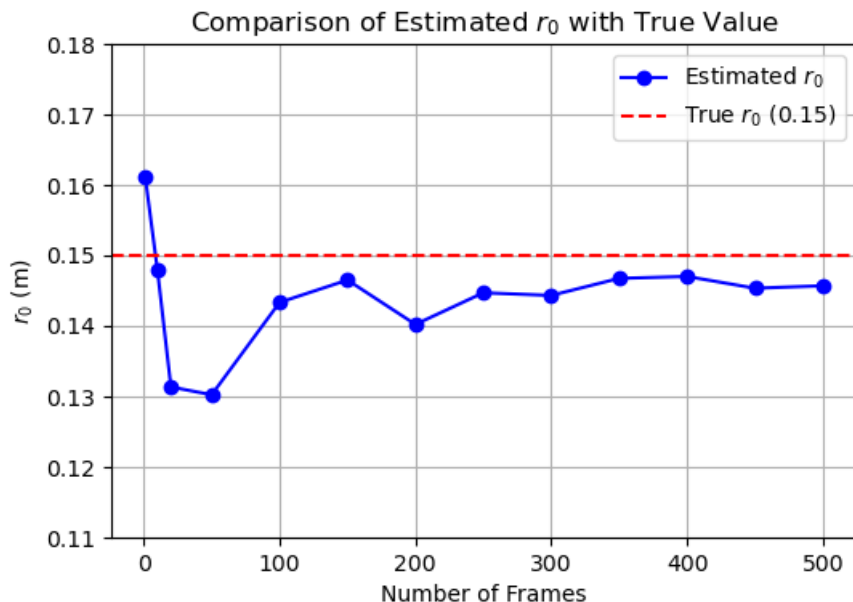


Figure 5.1: Comparison of estimated  $r_0$  with true value for a total of 500 iterations giving the average percentage error of 2.87%.

### Covariance Deviations for All Subapertures Over Time

This graph illustrates how the covariance deviations (in arcseconds) evolve over time for all subapertures during the simulation or measurement process. The deviations cluster tightly around zero, reflecting a system with stable performance and minimal fluctuation. The black line, representing the mean deviation, further confirms this temporal stability. However, occasional spikes in the deviations suggest transient effects, possibly caused by atmospheric turbulence anomalies, noise in the measurements, or other system perturbations. This temporal analysis is crucial for understanding the coherence of the wavefront sensor's performance and identifying potential calibration challenges.

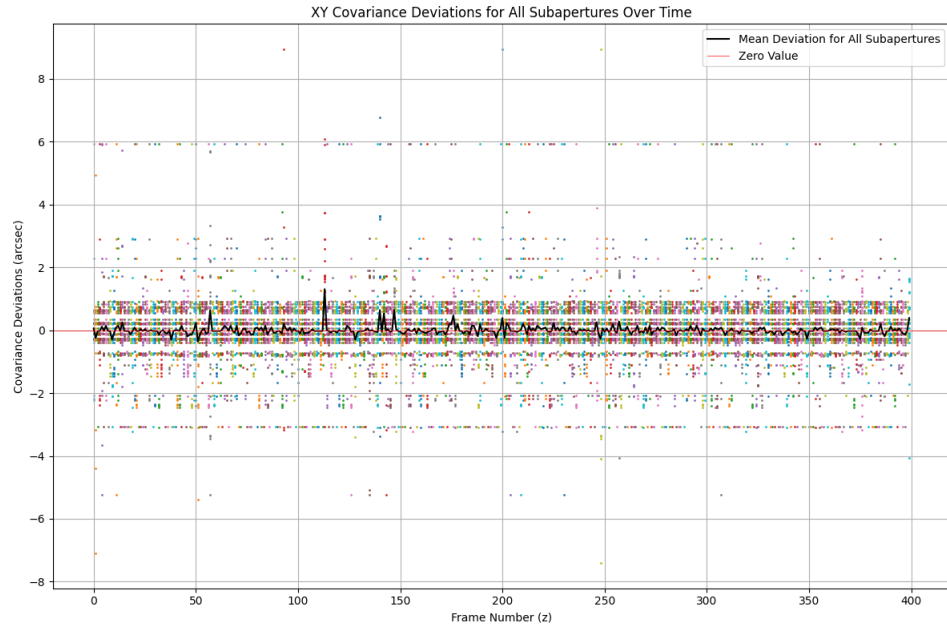


Figure 5.2: XY Covariance Deviations for All Subapertures Over Time. The thick line is the averaged spot motion for all of the subapertures. Reference methodology adapted from Jacques et al [33].

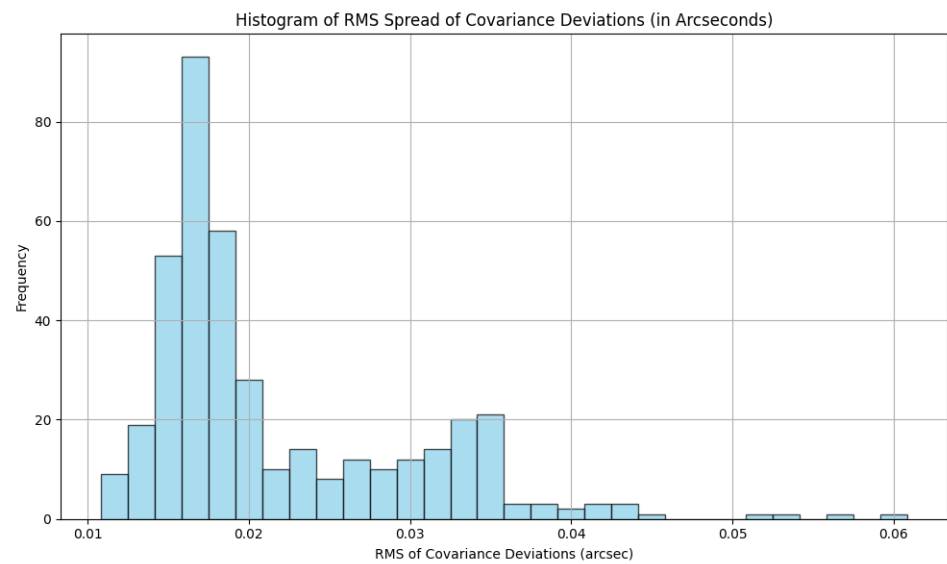


Figure 5.3: Histogram of RMS Spread of Covariance Deviations (in Arcseconds).

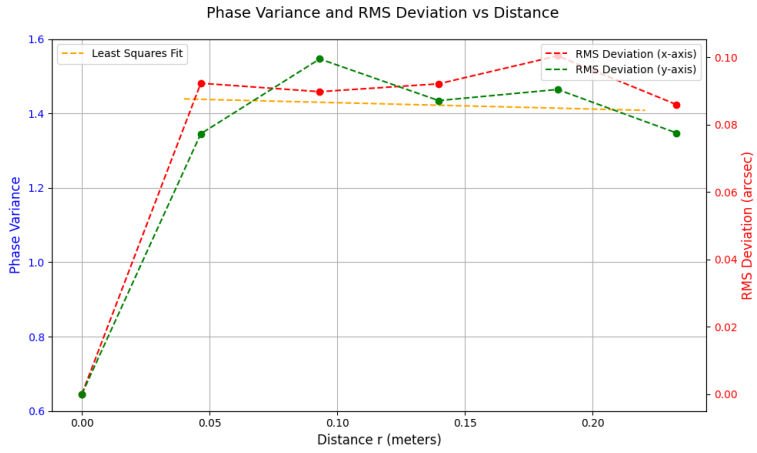


Figure 5.4: RMS Deviation from Reference vs Separation (X and Y) in Arcseconds. The yellow dotted lines show the corresponding least-squares fitted theoretical curve for a value of  $r_0$  equal to 0.15m.

### Histogram of RMS Spread of Covariance Deviations (in Arcseconds):

The histogram provides a statistical distribution of RMS deviations in arcseconds across all iterations. Most RMS values are concentrated within a narrow range, such as 0.01–0.03 arcseconds, indicating a well-performing system with minimal deviation. This distribution demonstrates that the majority of subapertures maintain stable covariance deviations. However, the presence of a tail in the histogram reveals occasional outliers, which may be attributed to rare atmospheric turbulence events or measurement noise. This analysis highlights the overall stability and occasional limitations in the system's performance.

### RMS Deviation from Reference vs Separation (X and Y) in Arcseconds:

This graph examines how the RMS deviations in the X and Y directions vary with the separation between subapertures. The observed trend of increasing RMS deviation at smaller separations suggests stronger covariance between nearby subapertures, consistent with the behavior expected in turbulence-dominated systems. At larger separations, the RMS deviations stabilize, indicating decorrelation between distant subapertures, likely due to the aperture size limiting their interaction. The theoretical least-square fit is also shown for comparison.

The differences between X and Y RMS deviations could point to anisotropic effects in the atmospheric turbulence or the optical system. This spatial analysis is valuable for characterizing the system's response to turbulence and subaperture interactions.

## 5.2 Optimization of the Number of Subapertures

As discussed in Section 3.1, impact of sampling is illustrated in Figure 5.5. Increasing the number of subapertures introduces a trade-off, where finer sampling comes at the expense of resolution. The normalization for the total photon count is done using the formula and example described in section 3.2.2.

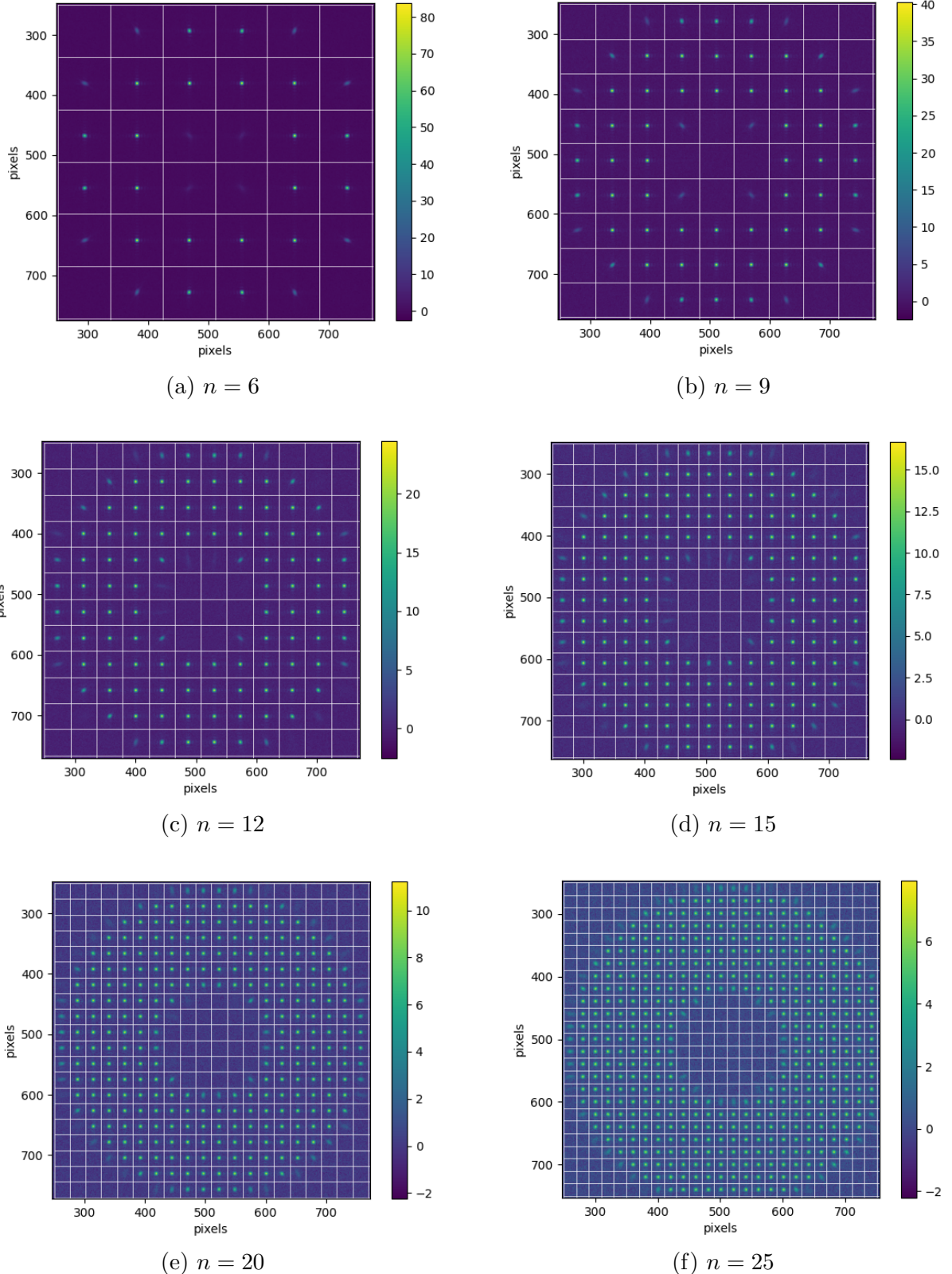


Figure 5.5: SHIMM spot pattern for number of subapertures  $n = 6, 9, 12, 15, 20$ , and  $25$  respectively. With increase in number of subapertures, the resolution decreases.

---

### 5.3 Future Directions

Understanding coherence time ( $\tau_0$ ) is important to characterizing atmospheric conditions since it quantifies the rate at which turbulence evolves. High-angular resolution techniques like interferometry and AO require this information [16]. For instance, in AO, the value of  $\tau_0$  denotes the duration that the AO correction process must function within for the correction to remain effective.

While the exact definition of  $\tau_0$  has been debated, it can be said that it represents the time required for optical phase variations of approximately  $\pi$  to develop at a specific location. Mathematically, this is expressed as  $D_\phi(\tau_0) = \pi^2$  [19].

Different approaches such as covariace map method and power spectrum method can be used to determine  $\tau_0$  as described by Perera et al. [26]. This process requires modelling of continuously evolving phase screen as described by Assemat et al. [3]. An application of this method can be seen in [AOtools](#).

Reconstruction of wavefront is an essential task for applications such as AO. Various methods and algorithms can be used for reconstructing the wavefront from the measured slopes. [6] [21] [20]

### 5.4 Conclusion

This study establishes a Shack-Hartmann based atmospheric turbulence monitor as an efficient and versatile tool for atmospheric turbulence profiling, demonstrating the reliability through theoretical modeling, numerical simulations, and noise impact assessments. The system's portable design, ease of deployment, and scalability make it an invaluable instrument for characterizing turbulence across diverse astronomical sites, facilitating better decision-making for telescope installation and operation.

The study highlights its robustness in varying environmental conditions, supported by its ability to measure Fried parameters. Additionally, the system's integration of noise-resilient algorithms ensures precision in measurements, even under challenging conditions.

Its potential extends beyond its current capabilities, paving the way for future advancements in multi-layer turbulence profiling and high-resolution adaptive optics calibration. Incorporating these enhancements will further optimize telescope performance by addressing more complex atmospheric scenarios. This project contributes to the development of affordable, precise tools essential for enhancing ground-based astronomical observations.

# Bibliography

- [1] The stratosphere. <https://www.windows2universe.org/earth/Atmosphere/stratosphere.html>.
- [2] Proper optical propagation library. <https://sourceforge.net/projects/proper-library/>.
- [3] François Assémat, Richard Wilson, and Eric Gendron. Method for simulating infinitely long and non stationary phase screens with optimized memory storage. *Optics Express*, 14(3):988, January 2006. doi: 10.1364/oe.14.000988. URL <https://doi.org/10.1364/oe.14.000988>.
- [4] R. Avila, J. L. Avils, R. W. Wilson, M. Chun, T. Butterley, and E. Carrasco. Lolas: an optical turbulence profiler in the atmospheric boundary layer with extreme altitude resolution. *Monthly Notices of the Royal Astronomical Society*, 387(4):1511–1516, June 2008. doi: 10.1111/j.1365-2966.2008.13386.x. URL <https://doi.org/10.1111/j.1365-2966.2008.13386.x>.
- [5] T. Butterley, R. W. Wilson, and M. Sarazin. Determination of the profile of atmospheric optical turbulence strength from slodar data. *Monthly Notices of the Royal Astronomical Society*, 369(2):835–845, May 2006. doi: 10.1111/j.1365-2966.2006.10337.x. URL <https://doi.org/10.1111/j.1365-2966.2006.10337.x>.
- [6] Gary A. Chanan. Principles of wavefront sensing and reconstruction. 2004. URL <https://api.semanticscholar.org/CorpusID:324274>.
- [7] Frederick R. Chromey. *To measure the sky*. Cambridge University Press, 2 edition, 2016.
- [8] Theodore De Karman and Leslie Howarth. On the statistical theory of isotropic turbulence. *Proceedings of the Royal Society of London a Mathematical and Physical Sciences*, 164(917):192–215, January 1938. doi: 10.1098/rspa.1938.0013. URL <https://doi.org/10.1098/rspa.1938.0013>.
- [9] Franklin W Diederich and Joseph A Drischler. Effect of spanwise variations in gust intensity on the lift due to atmospheric turbulence. *NACA Technical Note*, April 1957. URL [https://digital.library.unt.edu/ark:/67531/metadc56604/m2/1/high\\_res\\_d/19930084862.pdf](https://digital.library.unt.edu/ark:/67531/metadc56604/m2/1/high_res_d/19930084862.pdf).
- [10] Naber Francoise. *Encyclopedia Of Mathematical Physics*. S-Y Volume 5. Academic Press, 2006. URL [libgen.li/file.php?md5=3a55af8b7a79b77dcc0f24a9662ff7f1](http://libgen.li/file.php?md5=3a55af8b7a79b77dcc0f24a9662ff7f1).

- 
- [11] D. L. Fried. Statistics of a geometric representation of wavefront distortion. *Journal of the Optical Society of America*, 55(11):1427, November 1965. doi: 10.1364/josa.55.001427. URL <https://doi.org/10.1364/josa.55.001427>.
- [12] D. L. Fried. Optical resolution through a randomly inhomogeneous medium for very long and very short exposures. *Journal of the Optical Society of America*, 56(10):1372, October 1966. doi: 10.1364/josa.56.001372. URL <https://doi.org/10.1364/josa.56.001372>.
- [13] Joseph W. Goodman and Lorenzo M. Narducci. *Statistical Optics*, volume 39. 10 1986. doi: 10.1063/1.2815179. URL <https://doi.org/10.1063/1.2815179>.
- [14] Michael Goodwin, Charles Jenkins, Peter Conroy, and Andrew Lambert. Observations of ground-layer turbulence. *Proceedings of SPIE, the International Society for Optical Engineering/Proceedings of SPIE*, 7015:701549, June 2008. doi: 10.1117/12.787732. URL <https://doi.org/10.1117/12.787732>.
- [15] J.W. Hardy. *Adaptive Optics for Astronomical Telescopes*. Oxford series in optical and imaging sciences. Oxford University Press, 1998. ISBN 9780195090192. URL [https://books.google.co.in/books?id=-0aAWyckS\\_8C](https://books.google.co.in/books?id=-0aAWyckS_8C).
- [16] A. Kellerer and A. Tokovinin. Atmospheric coherence times in interferometry: definition and measurement. *aap*, 461(2):775–781, January 2007. doi: 10.1051/0004-6361:20065788.
- [17] Victor Kornilov, Andrei A. Tokovinin, Olga Vozyakova, Andrei Zaitsev, Nicolai Shatsky, Serguei F. Potanin, and Marc S. Sarazin. Mass: a monitor of the vertical turbulence distribution. *Proceedings of SPIE, the International Society for Optical Engineering/Proceedings of SPIE*, 4839:837, February 2003. doi: 10.1117/12.457982. URL <https://doi.org/10.1117/12.457982>.
- [18] John E. Krist. Proper: an optical propagation library for idl. *Proceedings of SPIE, the International Society for Optical Engineering/Proceedings of SPIE*, 6675:66750P, August 2007. doi: 10.1117/12.731179. URL <https://doi.org/10.1117/12.731179>.
- [19] A. Labeyrie, S. G. Lipson, and P. Nisenson. *An Introduction to Optical Stellar Interferometry*. Cambridge University Press, 2006.
- [20] V. P. Lukin, N. N. Botygina, O. N. Emaleev, and P. A. Konyaev. Wavefront sensors and algorithms for adaptive optical systems. *Proceedings of SPIE, the International Society for Optical Engineering/Proceedings of SPIE*, 7736:773659, July 2010. doi: 10.1117/12.856650. URL <https://doi.org/10.1117/12.856650>.
- [21] Iacopo Mochi and Kenneth A. Goldberg. Modal wavefront reconstruction from its gradient. *Applied Optics*, 54(12):3780, April 2015. doi: 10.1364/ao.54.003780. URL <https://doi.org/10.1364/ao.54.003780>.
- [22] James Osborn. *Profiling the turbulent atmosphere and novel correction techniques for imaging and photometry in astronomy*. PhD thesis, 2010. URL <https://api.semanticscholar.org/CorpusID:115620263>.

- 
- [23] James Osborn, Richard Wilson, Timothy Butterley, Harry Shepherd, and Marc Sarazin. Profiling the surface layer of optical turbulence with slodar. *Monthly Notices of the Royal Astronomical Society*, page no, May 2010. doi: 10.1111/j.1365-2966.2010.16795.x. URL <https://doi.org/10.1111/j.1365-2966.2010.16795.x>.
- [24] Bridget O'Donovan, John S. Young, Peter J. Warner, David F. Buscher, Donald M. A. Wilson, Roger C. Boysen, E. B. Seneta, and James Keen. Dimmwit: comparing atmospheric seeing values measured by a differential image motion monitor, which is transportable, and coast. *Proceedings of SPIE, the International Society for Optical Engineering/Proceedings of SPIE*, February 2003. doi: 10.1117/12.459761. URL <https://doi.org/10.1117/12.459761>.
- [25] Damian Peach. Atmospheric seeing information. <http://www.damianpeach.com/seeing1.htm>.
- [26] Saavidra Perera. *SHIMM: a low-cost portable seeing monitor for astronomical observing sites*. PhD thesis, January 2018. URL <http://etheses.dur.ac.uk/12640/>.
- [27] Saavidra Perera, Richard W. Wilson, James Osborn, and Tim Butterley. Shimm: a seeing and turbulence monitor for astronomy. *Proceedings of SPIE, the International Society for Optical Engineering/Proceedings of SPIE*, 9909:99093J, July 2016. doi: 10.1117/12.2231680. URL <https://doi.org/10.1117/12.2231680>.
- [28] Ben C Platt and Roland Shack. History and principles of shack-hartmann wavefront sensing. *Journal of Refractive Surgery*, 17(5), September 2001. doi: 10.3928/1081-597x-20010901-13. URL <https://doi.org/10.3928/1081-597x-20010901-13>.
- [29] J.-l. Prieur, G. Daigne, and R. Avila. Scidar measurements at pic du midi. *Astronomy and Astrophysics*, 371(1):366–377, May 2001. doi: 10.1051/0004-6361:20010279. URL <https://doi.org/10.1051/0004-6361:20010279>.
- [30] François Roddier. *Adaptive optics in astronomy*. Cambridge University Press, June 1999.
- [31] M. Sarazin and F. Roddier. The eso differential image motion monitor. *Astronomy and Astrophysics*, 227(1):294–300, January 1990. URL <https://ui.adsabs.harvard.edu/abs/1990A&A...227..294S/abstract>.
- [32] H. W. Shepherd, J. Osborn, R. W. Wilson, T. Butterley, R. Avila, V. S. Dhillon, and T. J. Morris. Stereo-scidar: optical turbulence profiling with high sensitivity using a modified scidar instrument. *Monthly Notices of the Royal Astronomical Society*, 437(4):3568–3577, November 2013. doi: 10.1093/mnras/stt2150. URL <https://doi.org/10.1093/mnras/stt2150>.
- [33] D. St-Jacques, G. C. Cox, J. E. Baldwin, C. D. Mackay, E. M. Waldram, and R. W. Wilson. The jose atmospheric seeing monitor at the william herschel telescope. *Monthly Notices of the Royal Astronomical Society*, 290(1):66–74, September 1997. doi: 10.1093/mnras/290.1.66. URL <https://doi.org/10.1093/mnras/290.1.66>.

- 
- [34] A. Tokovinin. Turbulence profiles from the scintillation of stars, planets, and moon. *Revista Mexicana De Astronomia Y Astrofisica Conference Series*, 31:61–70, October 2007. URL <https://ui.adsabs.harvard.edu/abs/2007RMxAC..31...61T/abstract>.
  - [35] A. Tokovinin and V. Kornilov. Accurate seeing measurements with mass and dimm. *Monthly Notices of the Royal Astronomical Society*, 381(3):1179–1189, October 2007. doi: 10.1111/j.1365-2966.2007.12307.x. URL <https://doi.org/10.1111/j.1365-2966.2007.12307.x>.
  - [36] Andrei Tokovinin. The elusive nature of “seeing”. *Atmosphere*, 14(11):1694, November 2023. doi: 10.3390/atmos14111694. URL <https://doi.org/10.3390/atmos14111694>.
  - [37] J. Vernin and F. Roddier. Experimental determination of two-dimensional spatiotemporal power spectra of stellar light scintillation evidence for a multilayer structure of the air turbulence in the upper troposphere. *Journal of the Optical Society of America*, 63(3):270, March 1973. doi: 10.1364/josa.63.000270. URL <https://doi.org/10.1364/josa.63.000270>.
  - [38] R. W. Wilson. Slodar: measuring optical turbulence altitude with a shack-hartmann wavefront sensor. *Monthly Notices of the Royal Astronomical Society*, 337(1):103–108, November 2002. doi: 10.1046/j.1365-8711.2002.05847.x. URL <https://doi.org/10.1046/j.1365-8711.2002.05847.x>.

# Appendix

## Codes for simulation

```

#----- Parameters for simulation -----
conf=dict(
    diam             = 0.2794,      # (meters)
    focal_ratio     = 10.0,        # f/
    wavelength      = 550e-9,      # (meters)
    gridsize         = 512,         # Simulation grid for primary
    sec_obs          = 0.34,        # Secondary obscuration fraction
    ,
    scale            = 1,
)

#for lenslet
d_pitch           = 0.3 * 1e-3, # pitch width
focal_length1     = 0.0142,      # focal length of lenslet(m)
gridsize2          = 64,          # Simulation grid for lenslet
)

#----- Calculating flux -----
import numpy as np

def calc_flux(area, app_mag, ref_flux, dll):
    Jy_photon = 1.51e7 * area * dll
    flux = 10**(-0.4 * app_mag)*ref_flux*Jy_photon
    return flux

r2    = 0.2794 / 2
r1    = 0.09525 / 2
area  = np.pi*(r2**2 - r1**2)
a_mag = 10
ref_flux = 3640
dll   = 0.16

n_photons = calc_flux(area, a_mag, ref_flux, dll)

Output:
Number of photons/second in V band: 47652.49616658752
Apparent magnitude : 10

#----- Proper simulation -----
import proper

aperture          = 0.2794          # meter
wavelength        = 550e-9          # meter
gridsize          = 1024

```

---

```

beam_ratio      = 0.3                      # beam diamter fraction
focal_ratio    = 10                         # f/#
focal_length   = aperture * focal_ratio

wfo = proper.prop_begin(aperture, wavelength, gridsize, beam_ratio)
proper.prop_circular_aperture(wfo, aperture/2)
proper.prop_lens(wfo, focal_length)
proper.prop_propagate(wfo, focal_length)
(psf,sampling) = proper.prop_end(wfo)

# ----- RESIZE IMAGE -----
def resize_img(img, new_size, preserve_range=True, mode='reflect',
               anti_aliasing=True):
    requirement = "new_size must be an int or a tuple/list of size 2."
    assert type(new_size) in [int, tuple, list], requirement
    if type(new_size) is int:
        new_size = (new_size, new_size)
    else:
        assert len(new_size) == 2, requirement
    assert img.ndim in [2, 3], 'image must be a frame (2D) or a cube (3D)'
    if img.ndim == 3:
        new_size = (len(img), *new_size)
    if new_size != img.shape:
        with warnings.catch_warnings():
            warnings.simplefilter("ignore")
            img = np.float32(resize(np.float32(img), new_size, mode=
                                      mode,
                                      preserve_range=preserve_range,
                                      anti_aliasing=anti_aliasing))
    return img

# ----- PAD IMAGE -----
def pad_img(img, padded_size, pad_value=0):
    requirement = "padded_size must be an int or a tuple/list of size 2."
    assert type(padded_size) in [int, tuple, list], requirement
    if type(padded_size) is int:
        (x1, y1) = (padded_size, padded_size)
    else:
        assert len(padded_size) == 2, requirement
        (x1, y1) = padded_size
    (x2, y2) = img.shape
    # determine padding region
    assert not (x1 < x2 or y1 < y2), "padding region cannot be smaller than image size."
    dx = int((x1 - x2) / 2)
    dy = int((y1 - y2) / 2)
    padx = (dx, dx) if (x1 - x2) % 2 == 0 else (dx + 1, dx)
    pady = (dy, dy) if (y1 - y2) % 2 == 0 else (dy + 1, dy)
    # pad image
    img = np.pad(img, [padx, pady], mode='constant', constant_values=
                pad_value)
    return img

```

---

```

----- Photocenter calculation -----
def photocenter(image, t=0.1):
    imax = np.percentile(image, 99.95)
    image -= t * imax
    image *= image > 0.0
    total = np.sum(image)
    X, Y = np.indices(np.shape(image))
    cx = (np.sum(Y * image) / total)
    cy = (np.sum(X * image) / total)
    return (int(cx), int(cy))

----- Covariance calculation -----
def covariance_observed(mean_y, mean_x, v_y, v_x, n):
    variance_sum = 0
    for i in range(n):
        variance_sum += (v_x[i] - mean_x) * (v_y[i] - mean_y)
    cov = variance_sum / (n - 1)
    observed_cov = np.mean(cov)
    return observed_cov

----- r0 calculation -----
def r_not(observed_cov, theoretical_cov, D):
    r_0 = {(observed_cov / theoretical_cov) ** (-3/5)} * D
    return r_0

-----READ - NOISE -----
def generate_read_noise(image, amount, gain):
    # Photons = Electrons / Gain
    shape = image.shape
    read_noise = noise_rng.normal(scale=amount / gain, size=shape)
    return read_noise

-----PHOTON - NOISE -----
def generate_photon_noise(image):
    photon_noise = np.sqrt(image)
    return photon_noise

```

The codes are provided in the GitHub link:

[https://github.com/LAXMIPRASOON/CBS\\_9th\\_sem\\_codes](https://github.com/LAXMIPRASOON/CBS_9th_sem_codes)

The link for downloading PROPER:

<https://sourceforge.net/projects/proper-library/>